A novel coupling algorithm for the electric field–structure interaction using a transformation method between solid and shell elements in a thin piezoelectric bimorph plate analysis

Prakasha Chigahalli Ramegowda, Daisuke Ishihara*, Tomoya Niho, Tomoyoshi Horie

Department of Mechanical Information Science and Technology,
Kyushu Institute of Technology, 680-4 Kawazu, Iizuka, Fukuoka, 820-8502, Japan

Abstract

Thin piezoelectric bimorph cantilever is increasingly employed throughout the field of actuator and sensor applications in the microelectromechanical system (MEMS). Generally for finite element analysis of piezoelectric bimorph cantilever, three–dimensional (3D) solid element can accurately take into account a linear or quadratic distribution of electric potential over the thickness for various electric configurations of the actuator and sensor applications. As the MEMS structures usually are quite thin and undergo large deformations, shell elements are very well suited for the structural discretization. This paper is focused on the development of a novel coupled algorithm to analyze the electromechanical coupling in a piezoelectric bimorph actuator and sensor using the shell and solid elements to simulate the structural and electric fields, respectively. The electric force induced by the inverse piezoelectric effect is transformed from the solid elements to the shell elements as an equivalent external force and moment, and the resultant displacements are transformed from the shell elements to the solid elements to evaluate the direct piezoelectric effect. Two different approaches were developed to analyze the electric–structure interaction. In the first approach, for each block Gauss–Seidel (BGS) iteration, multiple full Newton–Raphson (N–R) iterations are executed until the tolerance criteria are satisfied. In the second approach, the BGS and N–R loops are unified into a single loop. A piezoelectric bimorph actuator and sensor were analyzed for various electrical configurations to demonstrate the accuracy of the proposed method.

Keywords: Microelectromechanical Systems (MEMS), coupled algorithm, block Gauss–Seidel (BGS) method, piezoelectric effect, electromechanical coupling, electric field–structure interaction, piezoelectric bimorph actuator and sensor.

1. Introduction

The piezoelectric effect has been used in numerous applications since its discovery by the Curie brothers [1]. This effect is basically the interaction between the electrical and mechanical states in a material. Piezoelectricity, which can be subdivided into the direct and inverse piezoelectric effects, is widely used in both sensors and actuators in MEMS. Designing piezoelectricity-based MEMS sensors and actuators has been an ongoing process over the last few decades. The past decade has seen significant advances in the market growth of MEMS-based piezoelectric products [2], and a wide array of piezoelectric MEMS devices have been developed [3]. Generally, piezoelectric MEMS devices consist of a thin flexible unimorph or bimorph model. In particular, piezoelectric bimorphs [4] shown in Fig. 1 have been incorporated in various actuator applications [5–7] and sensor applications [8, 9]. The piezoelectric sensing effect can also be used for energy harvesting [10, 11].

Recently, the flexible wings of insect-like micro air vehicles [12, 13], which are robotic insects with flexible flapping wings are actuated by a piezoelectric bimorph actuator. Recent advances in the mechanics of flapping flight systems have been presented in Ref.[14].
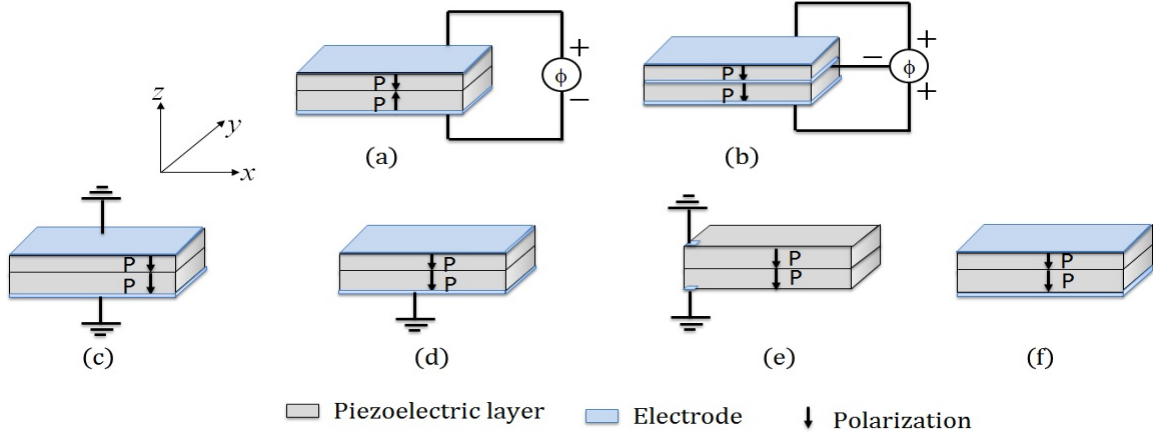
Piezoelectric bimorph actuators and sensors generally consist of two or three electrodes at the top, mid-surface (interface between the two piezoelectric layers) and bottom surfaces which are modeled using electric potential variables enabling to apply an electric field or to obtain sensor signals, respectively. These electrodes are conventionally made of the metal coating. Generally, the nodes with the electric degree of freedom (DOF) at the top, bottom and mid-surfaces of a piezoelectric bimorph FE model are regarded as an electrode

In piezoelectric bimorph actuator function, typically an electric potential is applied between the top, interface and bottom electrodes (see Fig. 1(a) and (b)). Thus, the loading is caused by an applied electric potential across the thickness. This results in a pure bending of the structure, where the electric potential varies almost linearly in the thickness direction [15–17]. Usually two different electric configurations are used in the piezoelectric actuator application [4, 18]. One is series connection in which the piezoelectric bimorph layers are usually polarized oppositely and the top electrode is applied a potential while the

*Corresponding author

Email addresses: prakasha@solid.mse.kyutech.ac.jp (Prakasha Chigahalli Ramegowda), ishihara@mse.kyutech.ac.jp (Daisuke Ishihara*), niho@mse.kyutech.ac.jp (Tomoya Niho), horie@mse.kyutech.ac.jp (Tomoyoshi Horie)

Fig. 1. Schematic of the electrical configurations of a piezoelectric bimorph cantilever FE model; a) bimorph actuator in a series configuration, b) bimorph actuator in a parallel configuration, c) bimorph sensor in a closed circuit configuration, d) bimorph sensor in a active–sensory mode configuration, e) bimorph sensor in a partial open circuit, f) bimorph sensor in a full open circuit. P refer to polarization.

bottom electrode is set to zero representing grounding, shown in Fig. 1(a). The other is parallel connection in which the piezoelectric layers are polarized parallel and both the top and bottom electrodes are applied a potential while the interface electrode is grounded, shown in Fig. 1(b). For the above mentioned electric configurations, the actuator surface becomes equipotential electrodes [19] wherein electric potentials have known prescribed values. This leads to a nearly linear variation of the electric potential across the thickness.

On the other hand, in piezoelectric sensor mode, when some mechanical force is applied on to the piezoelectric continuum, some electric voltage is induced in the piezoelectric material. Commonly, four types of electric configurations are employed, namely, closed circuit, closed and open circuit, partial open circuit, and full open circuit configuration. In the closed circuit configuration, the electric potentials of both the top and bottom electrodes are grounded (electric potentials have known prescribed values at all the nodes of both the top and bottom surfaces as shown in Fig. 1(c)). In the closed and open circuit configuration, the bottom electrode is grounded while the top electrode is open, this configuration is also known as active–sensory mode connection [19] wherein the electric potentials have known set values at the nodes of the bottom surface while the electric potentials are unknown at the nodes of the top surface as shown in Fig. 1(d). In the partial open circuit connection, the piezoelectric surfaces are directly exposed to the mechanical loading, but, to avoid unstable and floating electric potential distribution electrodes are deposited at the end of the piezoelectric layers and connected to the ground as shown in Fig. 1(e). In the full open circuit, the electrodes at the top and bottom surface are open (potentials are unknown at all the nodes of the top and bottom surfaces as shown in Fig. 1(f), a typical case in many piezoelectric energy harvesting [10, 11]. Either series or parallel polarization can be used. In the work of Benjeddou [20–22], Kogle & Bucalem [15, 23], Wang [16], and Fernandes & Pouget [17], it is demonstrated that only a quadratic variation of the electric potential over the thickness can take into account the potential induced by the bending dom-

inant deformation in a piezoelectric bimorph sensor mode.

Zienkiewicz and Taylor [24] have classified interactions in a coupled system into two classes. In class 1, the coupling occurs on domain interfaces, and in class 2, it occurs through the constitutive governing equations of the system. Electromechanical coupling belongs to the latter class. There is a growing need for numerical methods to analyze the electromechanical coupling of the piezoelectric effect using finite element methods. In the past few years, there have been considerable research efforts toward the development of the finite element method (FEM) in the numerical modeling and simulation of MEMS devices [25–31]. A number of researchers have analyzed piezoelectric bimorph cantilever in MEMS devices using the FEM [5, 7, 9, 27]. It is imperative to develop a finite element formulation which can take into account both actuator and sensor effect of a thin layered piezoelectric bimorph. At the same time, FE formulation must take into account almost a linear variation of the electric potential across the thickness in a piezoelectric actuator mode and a nearly quadratic variation of induced electric potential across the thickness in a piezoelectric sensor made of a thin layered piezoelectric bimorph.

The development of finite elements for the analysis of piezoelectric systems was first presented by Allik and Hughes [32]. More details regarding piezoelectric finite elements, such as piezoelectric solid, shell, plate, and beam elements, can be found in the survey by Benjeddou [20]. This survey discusses a wide range of studies in which different piezoelectric solid elements have been used to analyze electromechanical coupling [6, 32–41]. The electric potential is quadratic in a piezoelectric solid element proposed in Refs. [33, 39–41] except [32, 34–38] for which it is linear. Multi–layered linear solid elements over the thickness direction can treat a quadratic variation of electric potential across the thickness. The major advantages of using 3D piezoelectric solid elements in the analysis of electromechanical coupling are that they can correctly take into account the electric charge distribution on both the top and bottom surfaces and accurately represent the linear or quadratic variation of the induced electric potential along the thickness direction. Most
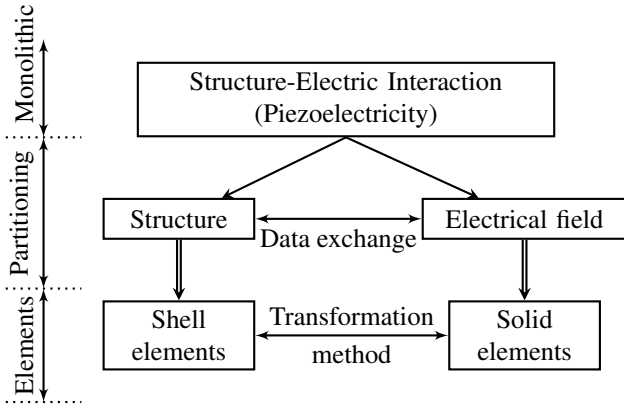
Fig. 2. Field decomposition of the structure–electric interaction using different types of finite elements.

importantly, all the above discussed electric configurations of both the actuator and sensor functions can be easily achieved with the 3D solid elements. However, the piezoelectric solid finite elements presented therein are inappropriate for the discretization of the structure in thin-layer MEMS actuators and sensors [42–44]. The computing cost of using solid elements to perform the structural analysis is larger.

Since MEMS piezoelectric composites are composed of thin layers and undergo large deformations, shell elements are very well suited for the structural discretization of these structures. Shell elements yield more accurate results than solid elements in terms of the dominant bending deformation. Furthermore, the computing cost of using shell elements to perform the structural analysis of these composites is much less than that of using solid elements. The finite element formulation of the shell elements for the geometric nonlinear analysis of thin structures is well established [45, 46]. Shear locking in the shell can be eliminated by using the mixed interpolation of tensorial components (MITC) approach [45–47]. However, modeling the electric contribution in the discretization procedure is a challenging task when using the conventional formulations of shell elements.

Only a few studies using piezoelectric shell elements [42, 48, 49] were reported in the survey by Benjeddou [20]. Some recently developed piezoelectric shell elements [15, 22, 50–52] have shown incompatible approximation spaces for the electrical fields, particularly in bending-dominated problems, as discussed in previous reports [53, 54]. Many piezoelectric shell elements are limited to actuator applications (see e.g.[55, 56]), so that it can not be used to analyze piezoelectric sensor function. Numerous piezoelectric shell element formulations [42, 52, 53, 57–59] assumes a linear variation of the electric potential over the thickness, this limits the applicability of the elements to a certain loading conditions only, because the induced electric potential by the bending deformation is quadratic in piezoelectric sensor mode. Some piezoelectric shell elements [15, 42, 53, 58–60] can be used to model both the actuator and sensor mode, provided one or two equipotential electrodes in the piezoelectric actuator and sensor surfaces. However, they are limited to a certain electric configuration because they require the equipo-

tential electrodes at the top and bottom surfaces. Since the electric potential serves as unknowns in an active–sensory configuration, they are modeled with a linear variation of the electric potential through the thickness [53], which leads to quite a wrong solution because the electromechanical coupling would be partial and would neglect the induced potential in sensor mode, as discussed in [20]. A few piezoelectric shell elements in Refs. [15, 22, 50, 60] uses a quadratic variation of electric potential over the thickness in the multi–piezoelectric layer structures for both the actuator and sensor analysis, provided at least one equipotential electrode in the piezoelectric actuator and sensor surfaces. In the formulations of Lammering & Mesecke–Rischmann [50], the electrodes located at the laminate interface are assumed to be grounded for both the actuator and sensor modeling, therefore limiting to certain electric configurations. The above-mentioned shortcomings of piezoelectric shell elements related to the electrical field discretization can be treated using the 3D solid elements.

In this study, the best features of solid and shell elements were combined to analyze the electrical and mechanical fields of the piezoelectric effect in thin-layer piezoelectric bimorph actuators and sensors. Importantly, the monolithic constitutive equations describing the piezoelectric effect were decomposed into the electrical and structural fields, enabling the use of different elements to solve the different fields. Field decomposition [61] enables the use of solid elements for electrical analysis and shell elements for structural analysis, as shown in Fig. 2. Since the electric field is solved using solid elements, the induced electric forces and the moment of these forces must be transformed as externally applied forces acting on to the shell elements to analyze the mechanical field. Conversely, because the structural field is solved using shell elements, the displacements obtained from the structural analysis of the shell elements must be transformed to the solid elements. Therefore, this paper proposes a novel transformation method for the electric force, the moment of the electric force, and the displacement transformation to exchange the variables between solid and shell elements in the direct and inverse piezoelectric analysis. In the present work, the BGS partitioned iterative coupling scheme [27] was used to apply the two types of finite elements (the solid elements for the electrical analysis and the shell elements for the structural analysis) in the developed transformation method. Two approaches of analyzing the dynamic and static behavior of the piezoelectric continuum are proposed using our transformation method. In the first approach, a full N–R iteration loop is executed inside the BGS loop; therefore, many N–R iterations are executed in each BGS iteration. In contrast, in the second approach, only one N–R iteration is executed in each BGS iteration, i.e., the BGS iteration loop and the full N–R iteration loop are unified in a single loop.

In summary, different from the previous methods, the proposed method can model both the actuator and sensor effect in a thin-layer piezoelectric bimorph beam for any electrical configurations with a quadratic variation of the electric potential across the thickness, a novel transformation method between the solid and shell elements accurately takes into account the electromechanical coupling for both the actuator and sensor

mode, and the field decomposition allows users to reuse the existing finite elements and its extensibility for multiphysics problems. The stability and accuracy of the two approaches are presented for a standard series-type and parallel type piezoelectric bimorph actuator. A sensor function is demonstrated for a piezoelectric bimorph with a closed circuit, combination of open and closed circuit, partial open circuit, and full open circuit configurations.

2. Coupled analysis method for the structure–electric interaction of piezoelectricity

2.1. Governing equations and finite element equations of the piezoelectric effect

For the sake of simplicity, the linear piezoelectric effect is assumed in this section. The electrostatic response of a piezoelectric continuum is governed by the equation of mechanical equilibrium and Maxwell's equation for a quasistatic electric field, which are respectively given as [62, 63]

$$\sigma_{ij,j} + f_i = \rho \ddot{u}_i, \tag{1}$$

$$D_{i,i} = 0, \tag{2}$$

where σ is the stress tensor, f is the body force vector, ρ is the mass density, $\ddot{u}$ is the acceleration vector, and D denotes the electric displacement vector. The constitutive equations of the linear piezoelectric effect can be written as

$$\sigma_{ij} = C_{ijkl}\epsilon_{kl} - e_{kij}E_k, \tag{3}$$

$$D_i = e_{ikl}\epsilon_{kl} + \varepsilon_{ik}E_k, \tag{4}$$

where ϵ is the strain tensor, C is the elastic tensor for constant electric field, e is the piezoelectric tensor, ε is the dielectric tensor for constant mechanical strains, and E denotes the electric field vectors. The strain tensor ϵ_{ij} and the electric field vector E_i are respectively derived from the mechanical displacement vector u_i and the scalar electric potential ϕ as

$$\epsilon_{ij} = \frac{1}{2}(u_{i,j} + u_{j,i}), \tag{5}$$

$$E_i = -\phi_{,i}. \tag{6}$$

To solve Eqs.(1) and (6) describing the piezoelectric body Ω, the following essential or natural mechanical and electrical boundary conditions on the boundary Γ of the body are prescribed:

$$u_i = u_i^\star \quad \text{on} \quad \Gamma_u \quad \text{and} \quad \phi = \phi^\star \quad \text{on} \quad \Gamma_\phi, \tag{7}$$

$$\sigma_{ij}n_j = f_i^\star \quad \text{on} \quad \Gamma_\sigma \quad \text{and} \quad D_i n_i = q^\star \quad \text{on} \quad \Gamma_q, \tag{8}$$

where $u_i^\star$ and $f_i^\star$ are the prescribed mechanical displacement and surface force components, respectively; $\phi^\star$ and $q^\star$ are the prescribed electric potential and surface charge, respectively; n_i is the outward unit normal vector. The piezoelectric constitutive equations (Eqs.(3) and (4)) can be written in matrix form as

$$\begin{bmatrix} \sigma \\ D \end{bmatrix} = \begin{bmatrix} \mathbf{C} & \mathbf{e} \\ \mathbf{e^T} & -\varepsilon \end{bmatrix} \begin{bmatrix} \epsilon \\ -\mathbf{E} \end{bmatrix}. \tag{9}$$
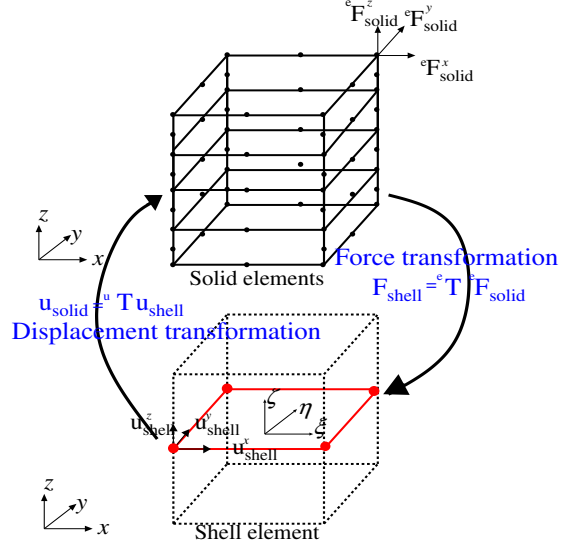

Fig. 3. Electric force and displacement transformation between the solid and the shell elements.

The weak forms of the elastic and electric balance laws Eqs.(1) and (2) are obtained using the method of weighted residuals, as described in [32, 62]. The semidiscrete equations of motion of linear piezoelectricity in the global coordinate system can be derived using the variation principle with the standard procedure of the FEM as [62]

$$\mathbf{M_{uu}\ddot{u}} + \mathbf{K_{uu}u} + \mathbf{K_{u\phi}\phi} = \mathbf{F}, \tag{10}$$

$$\mathbf{K_{u\phi}^T u} + \mathbf{K_{\phi\phi}\phi} = \mathbf{q}, \tag{11}$$

where $\mathbf{M_{uu}}$ is the mass matrix, $\mathbf{K_{uu}}$ is the global mechanical stiffness matrix of the structure, $\mathbf{u}$ is the global generalized mechanical displacements, $\mathbf{F}$ is the global external mechanical forces, ϕ represents the global electric potentials, $\mathbf{q}$ represents the global external surface density charges of the piezoelectric actuator, and a super-scripted T indicates the transpose of a matrix. Furthermore, the global piezoelectric stiffness matrix $\mathbf{K_{u\phi}}$ and the global dielectric stiffness matrix $\mathbf{K_{\phi\phi}}$ of the piezoelectric continuum are obtained by summing the contribution from each element. The extension of Eqs.(10) and (11) to the geometric nonlinear case is described in Section 2.4.

2.2. Shell structure formulation for geometric nonlinear effect

The large deformation formulation to capture the geometric nonlinear effects of the shell element is performed effectively by the use of an incremental formulation (a total Lagrangian formulation [64]) of the equations of motion. In Fig. 4, $^0x_i = $ Cartesian coordinates at time 0; $e_i = $ the local Cartesian system of orthogonal base vectors; $r_i = $ natural coordinates; $g_i = $ covariant base vector in natural coordinates; $u_i^k = $ the nodal point incremental displacements at time t; $^tV_1^k$ and $^tV_2^k$ are the vector normal's to the director vector $^tV_n^k$ at each node at time t; and α^k and β^k are the rotations of the director vector about $^tV_1^k$ and $^tV_2^k$. The director vector of the shell at time $t + \Delta t$ is updated by the finite rotation tensor, as described in [45].

4

In the total Lagrangian formulation we consider the principle of virtual work for the equilibrium at the configuration at time $t + \Delta t$

$$\int_{{}^0\Omega} {}^{t+\Delta t}_0\tilde{\sigma}_{ij} \, \delta \, {}^{t+\Delta t}_0\tilde{\epsilon}_{ij} \, d^0\Omega = {}^{t+\Delta t}W, \qquad (12)$$

where ${}^{t+\Delta t}_0\tilde{\sigma}_{ij}$ are the contravariant components of the 2nd Piola-Kirchhoff stress tensor at time $t + \Delta t$ but referred to the configuration at time 0, ${}^{t+\Delta t}_0\tilde{\epsilon}_{ij}$ are the covariant components of the Green-Lagrange strain tensor, and ${}^{t+\Delta t}W$ is the external virtual work and includes the work due to external surface traction and body forces. ${}^{t+\Delta t}_0\tilde{\sigma}_{ij}$, ${}^{t+\Delta t}_0\tilde{\epsilon}_{ij}$ are incrementally decomposed as described in [46, 65], and the tilde overbar denotes values measured in the covariant system. Substituting the decomposed stresses and strains into Eq.(12) gives the completely linearized equation of motion in a total Lagrangian formulation with convected coordinates [46],

$$\int_{{}^0\Omega} {}_0\tilde{C}^{ijkl} {}_0\tilde{e}_{kl}\delta_0\tilde{e}_{ij}d^0\Omega + \int_{{}^0\Omega} {}^t_0\tilde{\sigma}^{ij}\delta_0\tilde{\eta}_{ij}d^0\Omega$$
$$= {}^{t+\Delta t}W - \int_{{}^0\Omega} {}^t_0\tilde{\sigma}^{ij}\delta_0\tilde{e}_{ij}d^0\Omega, \qquad (13)$$

where ${}_0\tilde{e}_{ij}$ and ${}_0\tilde{\eta}_{ij}$ are linear and nonlinear strain increments of the GreenLagrange strain, respectively.

The MITC4 element, originally developed by Dvorkin and Bathe [46] is chosen in this work since it was widely used in practical engineering analysis of plates and shells. The MITC approach has a solid theoretical basis and also shown to be a reliable way of eliminating the shear locking of thin shells. In MITC approach, all strain components are evaluated in the standard manner [64], except for the transverse shear strains which are constructed employing separate interpolations in-order to eliminate shear and membrane locking. Here, assumed transverse shear strain field is introduced with the covariant components of the Green–Lagrangian strain tensor in the natural coordinate system. Now the assumed transverse shear strains $\tilde{\epsilon}^{AS}_{\alpha 3}$ are interpolated using the following equation [23, 46, 66]:

$$\tilde{\epsilon}^{AS}_{\alpha 3}(r_1, r_2) = \sum_{p=1}^{N_p} \tilde{h}^\alpha(r_1, r_2)\tilde{\epsilon}^{DI}_{\alpha 3}(r_1^p, r_2^p), \qquad (14)$$

where $\tilde{h}^\alpha(r_1, r_2)$ are the interpolation functions, and $\tilde{\epsilon}^{DI}_{\alpha 3}(r_1^p, r_2^p)$ are the transverse shear strain components at points $P_\alpha(r_1^p, r_2^p)$, $p = 1,...,N_p$, evaluated using the direct interpolations. Note that N_p is the number of interpolation points also known as tying points [46].

2.3. Transformation method between solid and shell elements

In this work, the piezoelectric structure is discretized into a finite number of shell elements to analyze the mechanical field [45, 46] and solid elements to analyze the electrical field [33]. The electric forces induced by the inverse piezoelectric effect in the solid elements must be transformed into forces and moments externally applied to the shell elements; similarly, the mechanical displacements must be transformed from the shell
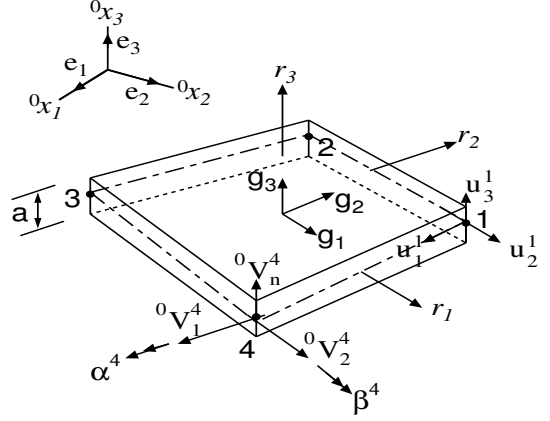

Fig. 4. Four–node isoparametric shell element

elements to the solid elements to evaluate the inverse piezoelectric effect, as shown in the Fig. 3. Therefore, a transformation method to exchange the mechanical and the electrical variables between the solid and shell elements is imperative.

2.3.1. Electric force and moment transformation from the solid to the shell elements

The standard bimorph actuator shown in Fig. 5 consists of a double layer of polyvinylidene difluoride (PVDF) piezoelectric layers joined together over their long surfaces with opposing polarization (P). Fig. 6 shows the regular grid-type mesh division of the bimorph actuator, and Fig. 7 shows the section highlighted by thick black lines in Fig. 6, which consists of a block of four solid elements and a shell element. The transformation equation that transforms the electric forces from the solid elements to the shell elements can be generally expressed as

$$\mathbf{F}_{\text{shell}} = {}^e\mathbf{T} \, {}^e\mathbf{F}_{\text{solid}}, \qquad (15)$$

where $\mathbf{F}_{\text{shell}}$ is the equivalent force vector at the shell elements, ${}^e\mathbf{F}_{\text{solid}}$ is the induced electric force vector in the solid elements, ${}^e\mathbf{T}$ is the transformation matrix, and the left-hand superscript e stand for "electric." As shown in Fig. 3, the induced electric forces in the solid elements ${}^e\mathbf{F}_{\text{solid}}$ are transformed as an equivalent force vector $\mathbf{F}_{\text{shell}}$ on to the shell elements. The electric forces induced in the solid elements by the inverse piezoelectric effect are calculated as

$$^e\mathbf{F}_{\text{solid}} = \mathbf{K}_{u\phi}\phi. \qquad (16)$$

Eqs.(15) and (16) are the general expressions of electric forces transformation from any type of solid elements to shell elements with regular and irregular meshes. The proposed method is quite general; however, for the purpose of simplicity the following assumptions were made in this study.

1. The top and bottom layers of the bimorph actuator have the same material properties and the same dimensions.
2. A shell midsurface (highlighted in red in Fig. 6) is placed at the interface of the two piezoelectric layers, and a regular grid-type mesh was used to discretize the shell midsurface.
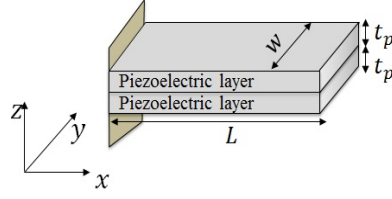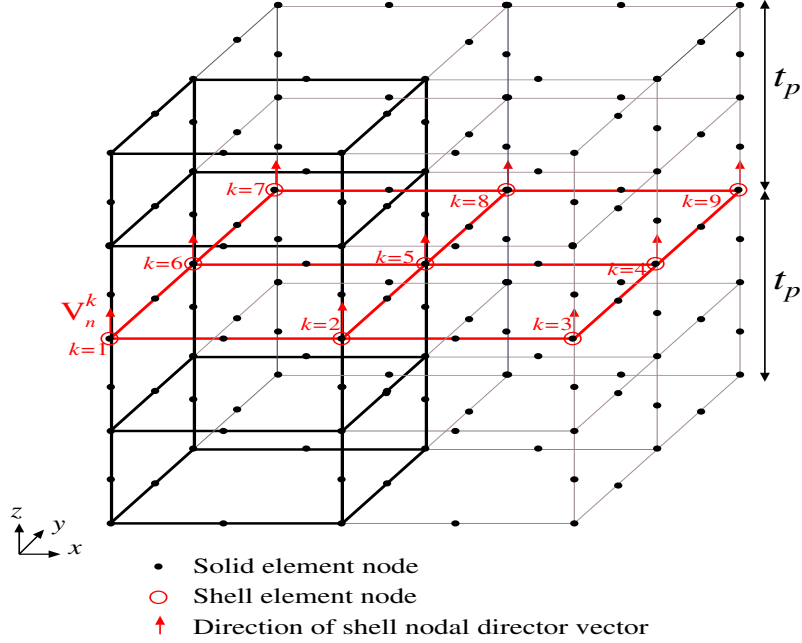
5

Fig. 5. Piezoelectric bimorph cantilever.

- •   Solid element node
- ○   Shell element node
- ↑   Direction of shell nodal director vector

Fig. 6. Regular grid-type meshing of a piezoelectric bimorph beam.

········▶ Induced electrical forces at n_r i.e., $^e F_{solid}^{n_r}$ are transformed to k

········▶ Induced electrical forces at n_s i.e., $^e F_{solid}^{n_s}$ are transformed to k

（a）Before force and moment transformation   （b） After force and moment transformation
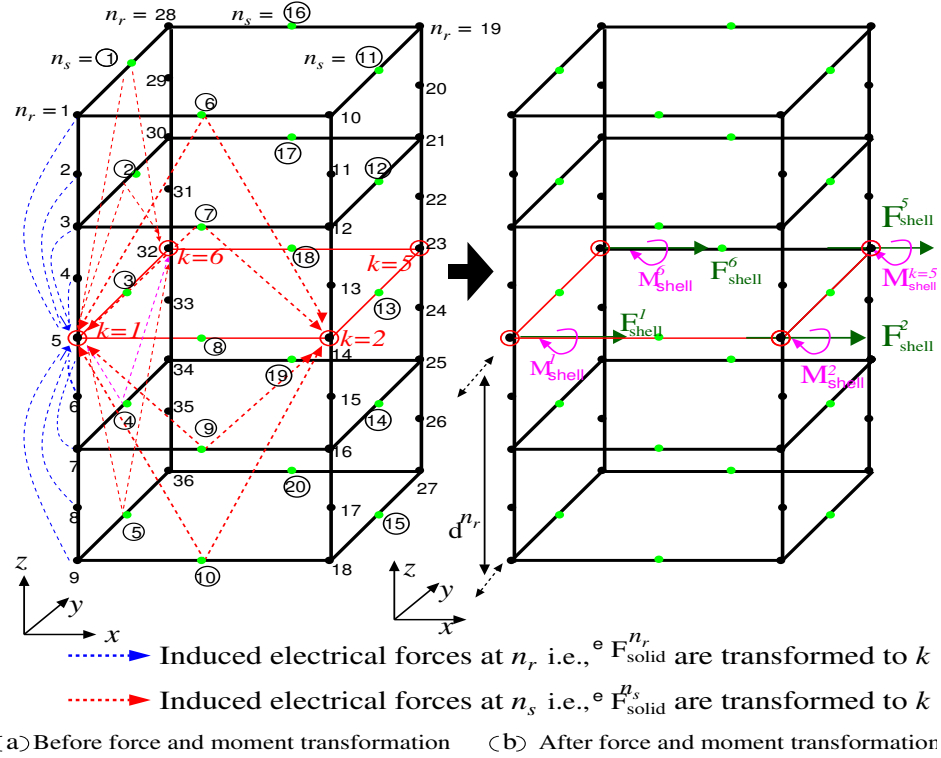
Fig. 7. Transformation of nodal electric forces and moments from solid to shell elements.

6

The equivalent externally applied forces at the shell node are given as

$$\mathbf{F}_{\text{shell}}^k = \sum_{n_r=1}^{N_r} {}^{\text{e}}\mathbf{F}_{\text{solid}}^{n_r} + \sum_{n_s=1}^{N_s} \frac{{}^{\text{e}}\mathbf{F}_{\text{solid}}^{n_s}}{2}, \qquad (17)$$

where $n_r = 1, \ldots, N_r$ are the indices of the solid element nodes that are located along the considered director vectors $\mathbf{V}_n^k$ of the shell nodes in the regular grid mesh shown in Fig. 6, N_r is the total number of these nodes, and ${}^{\text{e}}\mathbf{F}_{\text{solid}}^{n_r}$ is the induced nodal electric force vector at solid node n_r, as shown in Fig. 7. Similarly, $n_s = 1, \ldots, N_s$ are the indices of the solid element nodes that are located not along the considered director vector of the shell nodes but directly adjacent to it (see Fig. 7), N_s is the total number of these nodes, and ${}^{\text{e}}\mathbf{F}_{\text{solid}}^{n_s}$ is the induced nodal electric force vector at solid node n_s. The moment ${}^{\text{e}}\mathbf{M}_{\text{shell}}^k$ of the electric forces about the shell nodes can be easily calculated as

$$\mathbf{{}^{\text{e}}M}_{\text{shell}}^k = \sum_{n_r=1}^{N_r} (\mathbf{d}^{n_r} \times {}^{\text{e}}\mathbf{F}_{\text{solid}}^{n_r}) + \sum_{n_s=1}^{N_s} (\mathbf{d}^{n_s} \times \frac{{}^{\text{e}}\mathbf{F}_{\text{solid}}^{n_s}}{2}),$$
$$(18)$$

where $\mathbf{d}^{n_r}$ and $\mathbf{d}^{n_s}$ are the position vectors of the solid element nodes n_r and n_s, respectively, with respect to the shell mid-surface nodes. The components of the matrix ${}^{\text{e}}\mathbf{T}$ in Eq.(15) are then obtained from the electric force vector Eq.(17) and the moment of electric force vector Eq.(18).

Eqs.(17) and (18) correspond to the highlighted block of four solid elements and one shell element shown in Fig. 7. These equations should be summed for all other blocks in a regular grid mesh such as that shown in Fig. 7. As shown in Figures 6 and 7, the shell node $k = 1$, which is located in the corner of the mesh, has $N_r = 9$ solid nodes lying along $\mathbf{V}_n^1$ and $N_s = 10$ solid nodes adjacent to $\mathbf{V}_n^1$ contributing to the summations of the first and second terms in Eq.(17), respectively. Similarly, the shell node $k = 5$, which is shared among four neighboring shell elements in Fig. 6, has $N_r = 9$ and $N_s = 20$, and the shell node $k = 6$, which is located at the junction of two neighboring shell elements, has $N_r = 9$ and $N_s = 15$.

2.3.2. Displacement transformation from shell to solid elements

After the electric forces and the moment of the electric forces have been transformed from the solid elements to the shell elements using Eq.(15), the nodal displacements and rotations in the shell can be evaluated in the global Cartesian coordinate system. The equation that relates the displacements from the shell elements to the solid elements can be generally expressed as

$$\mathbf{u}_{\text{solid}} = {}^{\text{u}}\mathbf{T}\mathbf{u}_{\text{shell}}, \qquad (19)$$

where ${}^{\text{u}}\mathbf{T}$ is the displacement transformation matrix.

The displacements of a material point in a shell element at time t with natural coordinates (r_i) are evaluated from the nodal point displacements of the shell elements using the interpolation function [46] at time t as,

$${}^t\boldsymbol{u}_i = h^k(r_1, r_2) {}^t\boldsymbol{u}_i^k + \frac{r_3}{2} a\, h^k(r_1, r_2)({}^t\mathbf{V}_{ni}^k - {}^0\mathbf{V}_{ni}^k), \quad (20)$$

where ${}^t\boldsymbol{u}_i^k$ is the shell nodal displacement vector at time t. The displacements of a material point in a shell element with natural coordinates at time t in Eq.(20) are mapped to the corresponding solid element node at time t. The total number of material points in the shell structure is equal to the total number of nodal points in the solid elements used for the discretization of the electric field. As shown in Fig. 7, there are 56 nodes in four solid elements; therefore, 56 material points are considered in the shell structure at the natural coordinate r_3 of a material point in a shell element, which corresponds to the Cartesian coordinate x_3 of the corresponding solid element nodal point. The components of the matrix ${}^{\text{u}}\mathbf{T}$ are obtained from the interpolation function given in Eq.(20). As illustrated in Fig. 3, the resultant displacements in the shell elements $\mathbf{u}_{\text{shell}}$ are transformed to the solid elements.

2.4. Piezoelectric nonlinear dynamic analysis

In this section, the linear finite element equations of the piezoelectric effect given in Section 2.1 are extended to the geometric nonlinear case. Important earlier work on the evaluation of the performance of coupled finite element algorithms for the linear piezoelectric effect using the monolithic coupling and partitioned iterative schemes can be found in [27]. The BGS partitioned iterative coupling algorithm for the linear piezoelectric effect from our previous study [27] is extended here to the geometric nonlinear case. In the BGS coupling scheme, an updated electric potential is used in every iteration to evaluate the mechanical displacements. In this study, the BGS algorithm was used to couple the electrical field variables in the solid elements and the mechanical field variables in the shell elements.

2.4.1. Nonlinear structure–electric coupling scheme in the piezoelectric effect

The general expressions of the linearized coupled equations for the nonlinear structure–electric interaction in the piezoelectric effect are given as follows.
For the electrical field: The electrical field is solved as

$${}^{t+\Delta t}\mathbf{K}_{\phi\phi}^{(b)}\, {}^{t+\Delta t}\phi^{(b)} = {}^{t+\Delta t}\mathbf{q} - {}^{t+\Delta t}\mathbf{K}_{\phi u}^{(b)}\, {}^{t+\Delta t}\mathbf{u}^{(b-1)}, \quad (21)$$

where b indicates the current BGS iteration. The solution for the electric potential ${}^{t+\Delta t}\phi^{(b)}$ in Eq.(21) in each iteration is derived from the mechanical displacements ${}^{t+\Delta t}\mathbf{u}^{(b-1)}$ of the previous iteration.

For the structure: The equation used in the TL formulation with the full N–R iteration is

$${}^{t+\Delta t}_0\hat{\mathbf{K}}_{uu}^{(i-1)(b)}\, \boldsymbol{\Delta}\mathbf{u}^{(i)(b)} = \Delta\mathbf{R} - {}^{t+\Delta t}\mathbf{K}_{u\phi}^{(b)}\, {}^{t+\Delta t}\phi^{(b)}, \quad (22)$$

where i indicates the full N–R iteration, $\Delta\mathbf{R}$ is the out-of-balance force vector, and $\boldsymbol{\Delta}\mathbf{u}^{(i)(b)}$ is the incremental displacement at each BGS and N–R iteration in a time step. The last term on the right-hand side of Eq.(22) is the 3D electric force vector. The effective stiffness matrix is defined as

$${}^{t+\Delta t}_0\hat{\mathbf{K}}_{uu}^{(i-1)(b)} = \frac{1}{\beta\Delta t^2}\mathbf{M} + {}^{t+\Delta t}_0\mathbf{K}_{uu}^{(i-1)(b)}, \qquad (23)$$

where ${}^{t+\Delta t}_{0}\mathbf{K}^{(i-1)(b)}_{\mathrm{uu}}$ is the tangent stiffness matrix [45, 46] corresponding to the configuration at time $t + \Delta t$ but measured in the configuration at time 0 during N–R iteration $i - 1$ and BGS iteration b. The out-of-balance force vector $\Delta\mathbf{R}$ in Eq.(22) is defined as

$$\Delta\mathbf{R} = {}^{t+\Delta t}\mathbf{R} - \mathbf{M}\Big\{a_0\big({}^{t+\Delta t}\mathbf{u}^{(i-1)} - {}^{t}\mathbf{u}\big) - a_1{}^{t}\dot{\mathbf{u}} - a_2{}^{t}\ddot{\mathbf{u}}\Big\} \\ - {}^{t+\Delta t}_{0}\mathbf{F}^{(i-1)}, \tag{24}$$

where ${}^{t+\Delta t}\mathbf{R}$ is the vector of the externally applied nodal point loads at time $t + \Delta t$; ${}^{t+\Delta t}_{0}\mathbf{F}^{(i-1)}$ is the vector of the internal forces corresponding to the configuration at time $t + \Delta t$ but measured in the configuration at time 0; and $a_0 = \frac{1}{\beta\Delta t^2}$, $a_1 = \frac{1}{\beta\Delta t}$, and $a_2 = (\frac{1}{2\beta} - 1)$ are the Newmark constants. The displacement approximation is corrected by

$$ {}^{t+\Delta t}\mathbf{u}^{(i)(b)} = {}^{t+\Delta t}\mathbf{u}^{(i-1)(b)} + \Delta\mathbf{u}^{(i)(b)}. \tag{25}$$

In an incremental formulation based on the iterative methods (ex. Newton–Raphson iteration), efficient and realistic convergence criteria should be used to terminate the nonlinear iterations. Here, we compare the amount of work done by the out–of–balance loads on the displacement increments during every N–R iteration (i.e. the increment in internal energy) to the initial internal energy increment in–order to terminate the N–R iterations [67]. Convergence is assumed to be reached when, with e_{tol} a preassigned energy tolerance [64, 67],

$$\Delta\mathbf{u}^{(i)(b)}\big({}^{t+\Delta t}\mathbf{R} - \mathbf{M}^{t+\Delta t}\ddot{\mathbf{u}}^{(i-1)} - {}^{t+\Delta t}_{0}\mathbf{F}^{(i-1)}\big) \\ \leq e_{tol}\big(\Delta\mathbf{u}^{(1)(b)}\big({}^{t+\Delta t}\mathbf{R} - \mathbf{M}^{t}\ddot{\mathbf{u}} - {}^{t}_{0}\mathbf{F}\big)\big). \tag{26}$$

The approximation of the accelerations and velocities in the Newmark time integration is applied as described by Bathe [64]. This paper proposes the following two approaches, described in Fig. 8, for the nonlinear dynamic analysis of the structure–electric interaction in a piezoelectric actuator:

1. *Approach 1:* <u>BGS iteration with the N–R loop</u>
   In a BGS iteration, full N–R equilibrium iterations are evaluated until the energy tolerance is satisfied [67], and several BGS iterations are executed in each time step until the preassigned relative tolerance criteria is satisfied for displacements and potentials [63]. Eqs.(21) and (25) correspond to Approach 1. The analysis flow of this approach is illustrated in Fig. 8 with the blue note.

2. *Approach 2:* <u>Unified BGS iteration and N–R loop</u>
   <u>Here, the BGS and N–R loops are unified into single loop, therefore, we call this approach as unified BGS iteration and N–R loop. In this approach, mathematically the number of BGS iterations and N–R iterations are the same. Note that the iterations in the nonlinear analysis are also called as nonlinear iterations, therefore, we use the term nonlinear iterations to indicate the BGS or N–R iterations in this approach. The analysis flow of unified BGS iteration and N–R loop approach is illustrated</u>

in Fig. 8 with the red note. For this approach, Eq.(25) is modified as

$$ {}^{t+\Delta t}\mathbf{u}^{(b)} = {}^{t+\Delta t}\mathbf{u}^{(b-1)} + \Delta\mathbf{u}^{(b)}. \tag{27}$$

2.4.2. Nonlinear structure–electric coupling scheme using the proposed transformation method

The model for the nonlinear structure–electric interaction described in the previous section is quite general. Here, the proposed transformation method presented in Section 2.3 is applied to the general nonlinear piezoelectric equations given in Section 2.4.1.

Electrical field analyzed in the solid elements: The electrical field in the solid elements is solved using Eq.(21) as

$$ {}^{t+\Delta t}\mathbf{K}^{(b)}_{\phi\phi}{}^{t+\Delta t}\boldsymbol{\phi}^{(b)}_{\mathrm{solid}} = {}^{t+\Delta t}\mathbf{q} - {}^{t+\Delta t}\mathbf{K}^{(b)}_{\phi\mathrm{u}}{}^{t+\Delta t}\mathbf{u}^{(b-1)}_{\mathrm{solid}}. \tag{28}$$

The displacements ${}^{t+\Delta t}\mathbf{u}^{(b-1)}_{\mathrm{solid}}$ in the solid elements are obtained using the relation given in Eq.(19). Substituting Eq.(19) into Eq.(28) yields the electric potential in the solid elements as

$$ {}^{t+\Delta t}\mathbf{K}^{(b)}_{\phi\phi}{}^{t+\Delta t}\boldsymbol{\phi}^{(b)}_{\mathrm{solid}} = {}^{t+\Delta t}\mathbf{q} - {}^{t+\Delta t}\mathbf{K}^{(b)\,\mathrm{u}}_{\phi\mathrm{u}}\mathbf{T}\,{}^{t+\Delta t}\mathbf{u}^{(b-1)}_{\mathrm{shell}}. \tag{29}$$

The matrices ${}^{t+\Delta t}\mathbf{K}^{(b)}_{\phi\phi}$, ${}^{t+\Delta t}\mathbf{K}^{(b)}_{\mathrm{u}\phi}$, and ${}^{t+\Delta t}\mathbf{K}^{(b)}_{\phi\mathrm{u}}$ are evaluated from the solid elements at each BGS iteration in every time step $t + \Delta t$.

Structural field analyzed in the shell elements: The incremental displacements in the shell elements are obtained using Eq.(22) as

$$ {}^{t+\Delta t}_{0}\hat{K}^{(i-1)(b)}_{\mathrm{uu}}\Delta\mathbf{u}^{(i)(b)}_{\mathrm{shell}} = \Delta\mathbf{R} - {}^{t+\Delta t}\mathbf{F}^{(i-1)(b)}_{\mathrm{shell}}. \tag{30}$$

Substituting the transformation equation given in Eq.(15) into Eq.(30) yields

$$ {}^{t+\Delta t}_{0}\hat{K}^{(i-1)(b)}_{\mathrm{uu}}\Delta\mathbf{u}^{(i)(b)}_{\mathrm{shell}} = \Delta\mathbf{R} - {}^{\mathrm{e}}\mathbf{T}\,{}^{t+\Delta t}\mathbf{F}^{(i-1)(b)}_{\mathrm{solid}}, \tag{31}$$

where $\Delta\mathbf{u}^{(i)(b)}_{\mathrm{shell}}$ is the incremental displacement in the shell element. The tangent stiffness matrix ${}^{t+\Delta t}_{0}\mathbf{K}^{(i-1)(b)}_{\mathrm{uu}}$ is calculated in the shell elements.

The displacement approximation in the shell elements is corrected using

$$ {}^{t+\Delta t}\mathbf{u}^{(i)(b)}_{\mathrm{shell}} = {}^{t+\Delta t}\mathbf{u}^{(i-1)(b)}_{\mathrm{shell}} + \Delta\mathbf{u}^{(i)(b)}_{\mathrm{shell}}. \tag{32}$$

Eqs.(30) and (32) yield the structure in the shell elements from the electric forces and moments transformed onto the shell elements, which are considered as externally applied equivalent forces, as described in Section 2.3.1.

Table 1: Material properties of PVDF used in the analysis of a piezoelectric bimorph [7] (the absolute permittivity $\varepsilon_0 = 8.854\,\mathrm{pF/m}$).

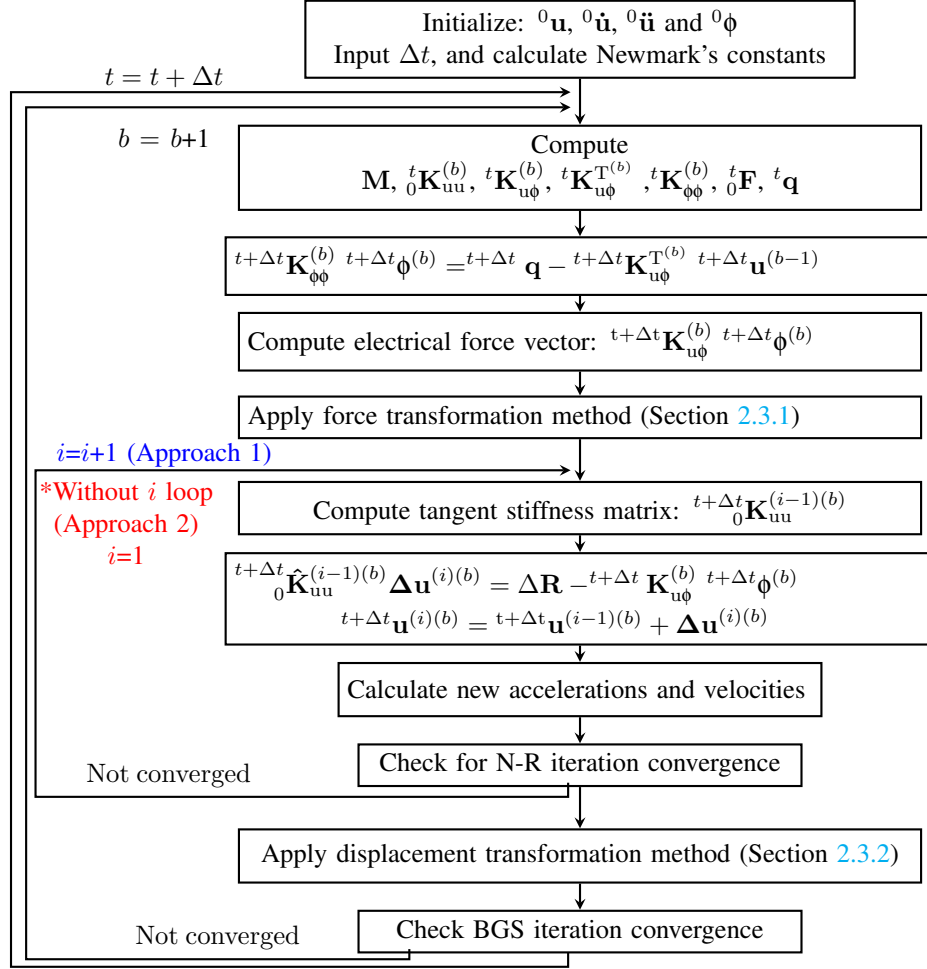|		
Young's modulus (GPa)	E_p	2.0
Density (kg/m^3)	ρ_p	1800
Poisson's ratio	v_p	0.29
Piezoelectric stress constant (C/m^2)	e_{31}	0.046
Piezoelectric strain constant (pC/N)	d_{31}	23.0
Electromechanical coupling factor	k_{31}	0.12

Fig. 8. Nonlinear dynamic piezoelectric analysis: Approaches 1 and 2.

(a) Bimorph actuator in series
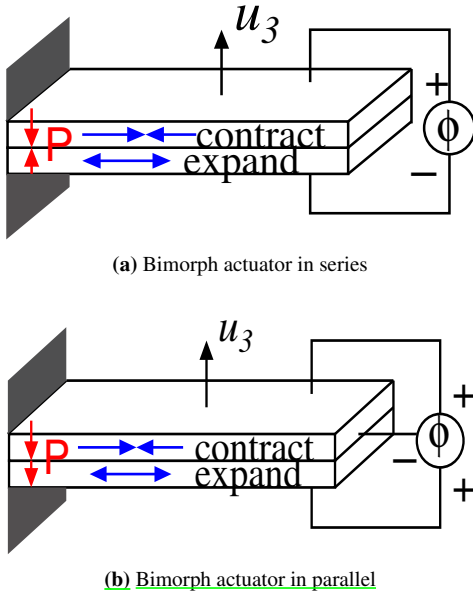

(b) Bimorph actuator in parallel

**Fig. 9.** Piezoelectric bimorph actuators subjected to external voltages .

3. Piezoelectric bimorph actuator: Results and discussions

3.1. Problem setup

The piezoelectric bimorph actuator shown in Fig. 5 consists of two piezoelectric layers joined together over their long surfaces. The beam has a length of $L = 100$ mm along x-axis, a width of $w = 1$ mm along y-axis, and a thickness of $t_p = 0.5$ mm along z-axis. The beam is fixed at $x = 0$. As shown in Fig. 9, two electrical loading cases are analyzed:

1. Series connection: Two layers of PVDF polarized along opposite transverse directions, see Fig. 9(a), uniform potential is applied on the top electrode with the bottom electrode being earthed.

2. Parallel connection: Two layers of PVDF polarized along same transverse directions, see Fig. 9(b), uniform potential applied on the top and bottom electrodes with the interface electrode being grounded.

For the electric configuration presented in Fig. 9, it is observed that under the potential load, the top and bottom layers of the piezoelectric bimorph actuator undergoes, respectively, contraction and expansion, and producing a pure bending in the upward direction.

9

(a) 3D solid elements for the electrical analysis.

(b) Shell elements for the structural analysis.
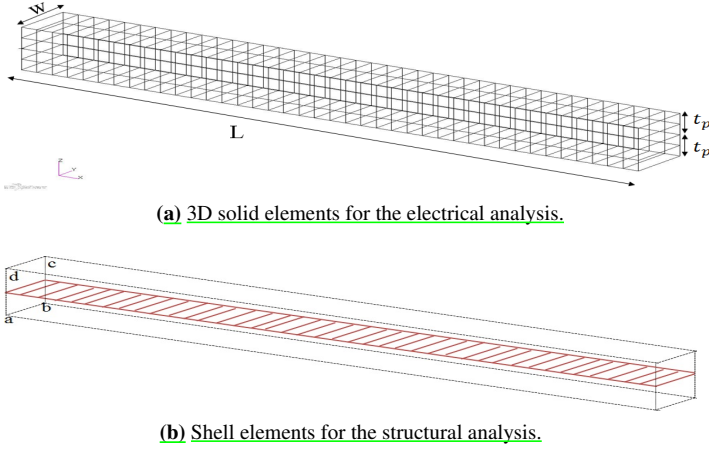
Fig. 10. Finite element mesh. Plane abcd is imposed fixed boundary conditions for the structural analysis ($t = 2t_p$ = 1mm, L = 100mm, and w = 1 mm).

3.2. Numerical setup

The meshes used for the electrical and structural analyses are shown in Fig. 10. The mesh for the electric analysis Fig. 10(a) consists of 20-node hexahedral elements with the numbers of the nodes and elements totaling 1343 and 160, respectively. The mesh for the structural analysis Fig. 10(b) consists of MITC4 shell elements [45, 47] with the numbers of nodes and elements totaling 82 and 40, respectively. In Fig. 10(a), the length of each solid element is 2.5 mm, the width of each solid element is 1mm, and the thickness of each solid element is 0.25mm. Therefore, the solid element aspect ratio is 10. The shell elements shown in Fig. 10(b) are positioned at the interface of the two piezoelectric layers discretized using 3D solid elements for electrical analysis as shown in Fig. 10(a). There are 40 shell elements in the x-direction; this number is consistent with the number of solid elements along the x-direction.

3.3. Static analysis of actuator function

3.3.1. Theoretical solution

The static deflection in thickness direction (z-direction) along length of the bimorph actuator (x-direction) is given as [18]

$$u_3(x) = \frac{3x^2}{4t_p}d_{31}E_3, \qquad (33)$$

where d_{31} is the piezoelectric strain constant, $E_3 = \phi/2t_p$ is an applied electric field for a series-type electrical connection and $E_3 = \phi/t_p$ for a parallel-type electrical connection and t_p is the thickness of each piezoelectric layers. Substituting the actuator dimensions and the material properties of the PVDF given in Table 1 into Eq.(33) with $x = L$ for $\phi = 1$ V across the thickness yields a static tip deflection of $u_3(L) = 0.3450$ μm for a series-type electrical connection and $u_3(L) = 0.690$ μm for a parallel-type electrical connection. The equivalent bending moment which is defined as the moment that can produce the same deflection in a piezoelectric bimorph actuator as an applied electric field, can be obtained as [4]

$$M_{eq} = \frac{wt^2E_p}{4}d_{31}E_3, \qquad (34)$$

where $t = 2t_p$ is the total thickness of the bimorph. For an applied voltage of $\phi = 1$ V with $E_3 = \phi/2t_p$ across the thickness yields

$$M_{eq} = 1.1500 \times 10^{-8} \text{ Nm}.$$

The first bending resonance $\omega_r^{(1)}$ for a piezoelectric bimorph actuator is given as [18]

$$\omega_r^{(1)} = \frac{1.875^2}{L^2}\sqrt{\frac{E_pI}{\rho_pA}}, \qquad (35)$$

where I is the second moment of area and A is the cross-sectional area. From Eq.(35), the resonance frequency for the first bending mode was obtained as 107.0 rad/s.

3.3.2. Numerical analysis

Here we will demonstrate the convergence properties, solution accuracy, and which approach is competitive from the viewpoint of the computational cost.

a) Convergence properties for approaches 1 and 2: Fig. 11(a) shows the convergence results for Approach 1, in which the first BGS iteration required three N–R iterations to satisfy the preassigned energy tolerance of $e_{tol} = 1.0 \times 10^{-12}$ and subsequent BGS iterations required two N–R iteration to satisfy this condition. Fig. 11(b) shows the relative error of the numerically obtained tip deflection using Approach 1 with respect to the theoretical solution given by Eq.(33). At BGS iteration 4, the tip deflection converged to within the set relative tolerance value of $\chi = 1 \times 10^{-5}$ in this approach. Totally nine nonlinear N–R iterations are necessary to obtain the converged solution.
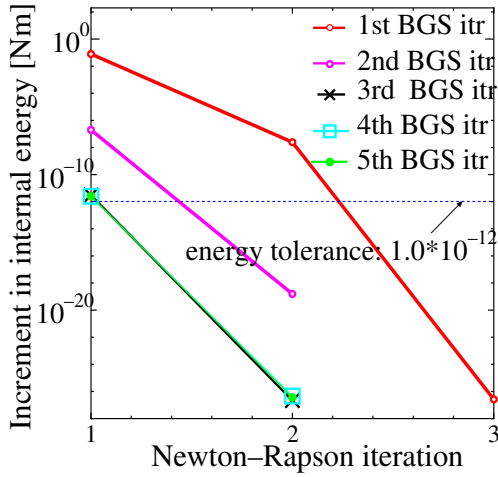
Fig. 12 shows the iteration convergence proprieties of Approach 2. Since the BGS and N–R loops are unified in this approach, we call the horizontal axis in Fig. 12 as nonlinear iteration. As shown here, the increment in internal energy and relative error in tip deflection are on the same vertical axis for each nonlinear iterations along the horizontal axis. By the fifth nonlinear iterations, the set energy tolerance condition, as well as the relative tolerance, was satisfied to perform static analysis of the numerical problem in Fig. 9(a).

b) Solution accuracy: The static deflections obtained using Approaches 1 and 2, the theoretical solution using Eq.(33), and the deflection at the nodes obtained by Tseng [6] and Wang et al. [7] are listed in Table 2 for a series and parallel connection. These cases are all under the condition of a unit input voltage. Tseng [6] modeled the piezoelectric continuum using solid hexahedral elements, which are too thick for the simulation of thin-layered MEMS devices. Wang et al. [7] used a piezoelectric plate element and applied the Guyan reduction method to condense the electric potential vectors. The results obtained from both of the proposed approaches show close agreement with the theory, and the accuracy of the present finite element solution is higher than that of the solutions obtained by Tseng [6] and Wang et al. [7]. The displacement of both the series and parallel actuator configurations are accurately predicted by the present model.

10

Table 2: Deflection of the piezoelectric PVDF bimorph actuator connected in series and parallel connection (for a unit applied voltage)

Location along the length(mm)	Deflection (μm)							
	Series connection					Parallel connection		
				Present			Present	
	Theory[18]	Tseng[6]	Wang[7]	Approach 1	Approach 2	Theory[18]	Approach 1	Approach 2
20	0.01380	0.01500	0.01390	0.01379	0.01378	0.0276	0.02746	0.02768
40	0.05520	0.05690	0.05470	0.05519	0.05511	0.1104	0.11040	0.11108
60	0.12420	0.13710	0.11350	0.12419	0.12413	0.2484	0.24880	0.24947
80	0.22080	0.23510	0.21980	0.22078	0.22079	0.4416	0.44268	0.44297
100	0.34500	0.35980	0.34160	0.34505	0.34510	0.6900	0.69200	0.69200

(a) N–R convergence in each BGS iteration.
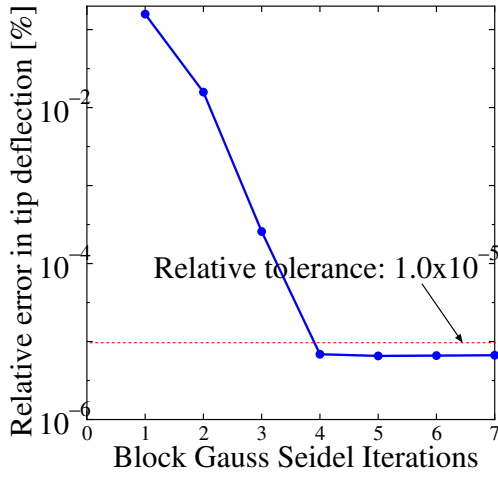
(b) BGS iteration convergence of the tip deflection.

Fig. 11. Iteration convergence analysis for the static case: Approach 1.

c) Demonstration of geometric nonlinear effect:
Fig. 13 shows the tip deflection of the bimorph actuator in series analyzed under various applied voltages. The purpose of this analysis is to demonstrate the superiority of the present nonlinear shell–solid method over our previous linear structure–electric field for the piezoelectric actuator analysis using purely solid [27] and linear theoretical solution [18]. From the current literature review, there are no nonlinear theoretical solu-
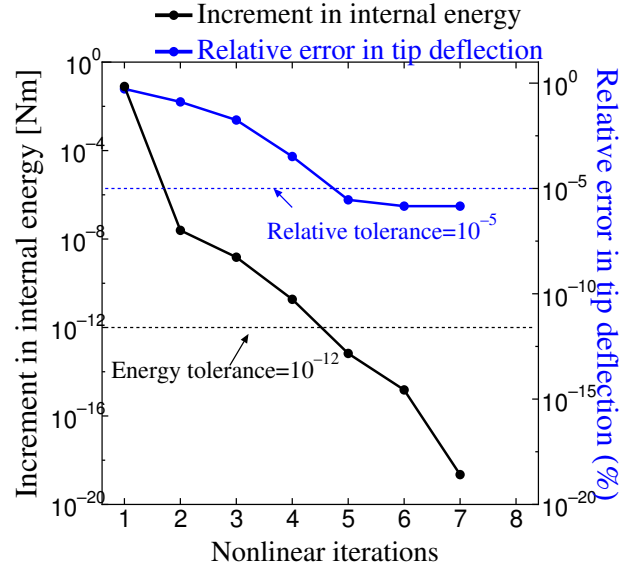

Fig. 12. Iteration convergence analysis for the static case: Approach 2.

tions for the deflection of the piezoelectric bimorph actuator. Therefore, blocking force F_b [4] corresponding to the induced electric forces for an applied voltage ϕ in a bimorph actuator is externally applied on to the nonlinear pure shell [45] to perform the structural analysis and the displacement obtained in the nonlinear pure shell is compared with the proposed shell–solid combination. The blocking force can be obtained as [4],

$$F_b = \frac{3wt^2 E_p}{8L} d_{31} E_3. \tag{36}$$

As shown in Fig. 13, the tip deflection at various voltage analyzed with linear solid–solid coincides with the linear theory. Also, at lower input bias voltages, in the elastic region, the deflections analyzed using present nonlinear shell–solid coincides with linear theory and linear solid–solid. However, at higher voltages, the proposed method shows the large deformation due to geometric nonlinear effect. The solution obtained with the pure shell using the blocking force corresponding to the respective input bias voltage is very close to that of the proposed method. This indicates that the proposed method accurately take into account the geometric nonlinear effect in a thin plate–like piezoelectric bimorph.
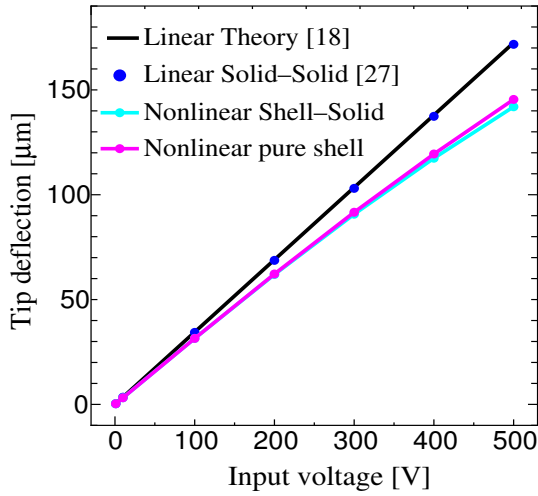
11

Fig. 13. Tip deflection of bimorph actuator in series at various input voltages.

d) Computational efficiency of shell–solid over solid–solid:
To demonstrate the computational efficiency and the solution accuracy to analysis thin plate–like flexible piezoelectric bimorph, dimensional parametric study for various length to thickness ratio (L/t) consists of different mesh divisions are presented in Fig. 14. For every L/t ratio, four mesh divisions with different structural and electrical degrees of freedoms (dof's) are shown. The thickness $t = 1$mm in $L/t = 300$, 200, and 100. The comparison of the structural dof's versus the relative error in tip deflection of the series connected piezoelectric bimorph actuator at bias voltage $\phi = 1V$ is made between the proposed nonlinear shell–solid and linear solid–solid.

As shown in Fig. 14, for very thin flexible piezoelectric bimorph actuator ($L/t = 300$), the nonlinear shell–solid method outperforms the linear solid–solid in terms of solution accuracy and structure dof's. Also, for each L/t ratio with mesh density indicated by magenta color, the solution accuracy is very close between the shell–solid and solid–solid. However, the structural dof's required by the solid–solid to achieve solution close to the shell–solid is very high. This indicates that the computational cost to analyze the structure is very high in solid–solid than that of shell–solid. It is shown that with the same in–plane division, the structural dof's of pure solid–solid is larger than that of the shell–solid. Therefore, proposed shell–solid is more computationally efficient. Among approaches 1 & 2, the BGS iteration with the N–R loop (Approach 1) requires nine nonlinear iterations to achieve convergence, on the other hand, the unified BGS iteration and N–R loop (Approach 2) require five nonlinear iterations to satisfy the convergence criteria. Therefore, the computation cost in the first approach is slightly higher than the second approach.

e) Electric potential across the thickness of the actuator:
The variation of the electric potential in the solid across the thickness direction for a series and parallel connection are presented in Fig. 15. The results confirm clearly that for a piezoelectric actuator mode, the variation of the electric potential
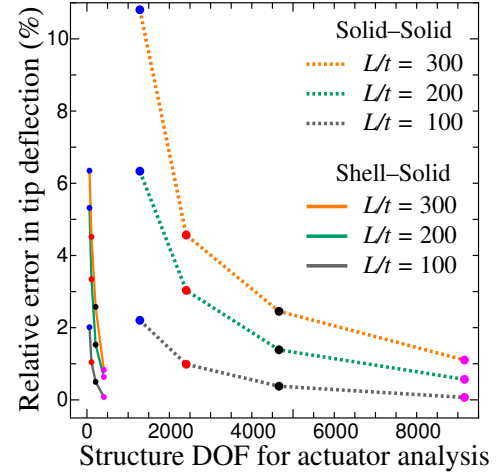
|	Number of nodes		Structure dof's	
	Solid–Solid	Shell–Solid	Solid–Solid	Shell–Solid
	Solid (Structure)	Shell (Structure)	Solid	Shell
●	428	12	1284	60
●	803	22	2409	110
●	1553	42	4659	210
●	3053	82	9159	410

Fig. 14. Solution accuracy versus structure dof's. Dotted lines indicates L/t ratio of bimorph cantilever for solid–solid mesh and solid lines indicates L/t ratio of bimorph cantilever for shell–solid mesh. Green, red, black, and magenta color dots indicates mesh densities and structure dof's.

varies almost linearly in the thickness direction, as previously discussed in [15, 16, 60]. Kogli & Bucalem in [15, 60] solved a piezoelectric bimorph actuator with a quadratic variation of electric potential over the thickness for a parallel electric configuration, their results clearly show that the electric potential varies almost linearly, because of the three equipotential electrodes at the top, bottom, and interface.

3.3.3. Validation of electric force and moment transformation

The purpose of this section is to validate the transformation of the electric forces and moments from the solid to the shell elements. The numerical problem described in Fig. 9(a) in the case with a unit static input voltage was considered. First, both the structure and electric field were solved using the solid elements to evaluate both the nodal displacements and the electric potential under the BGS coupling scheme [27]. Next, the electric force vector in the solid elements was calculated using Eq.(16). Then, the electric forces and moments were applied externally to the shell elements using the proposed force and moment transformation method described in Section 2.3.1 to obtain the mechanical displacements of the shell elements from the displacement interpolation function [46]. Finally, the displacements of the solid elements due to the piezoelectric effect were compared with the displacements of the shell obtained from the transformed electric forces and moments.

Fig. 16 shows the static deflection obtained by solving both
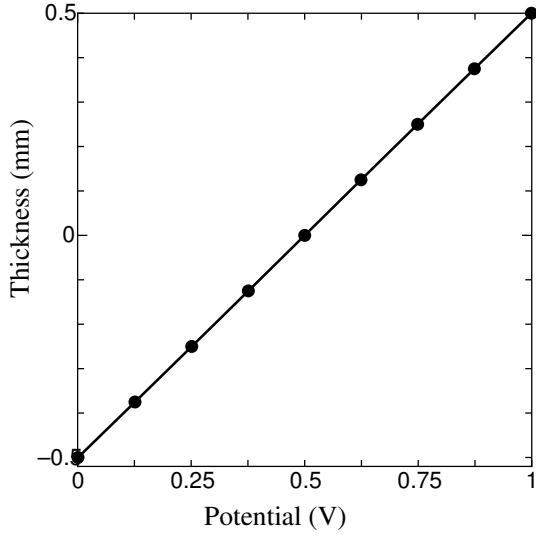
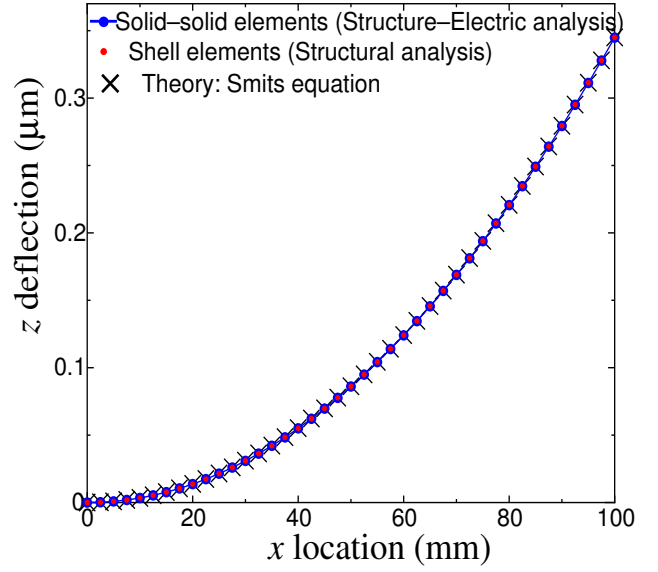**(a)** A series connection piezoelectric bimorph actuator.
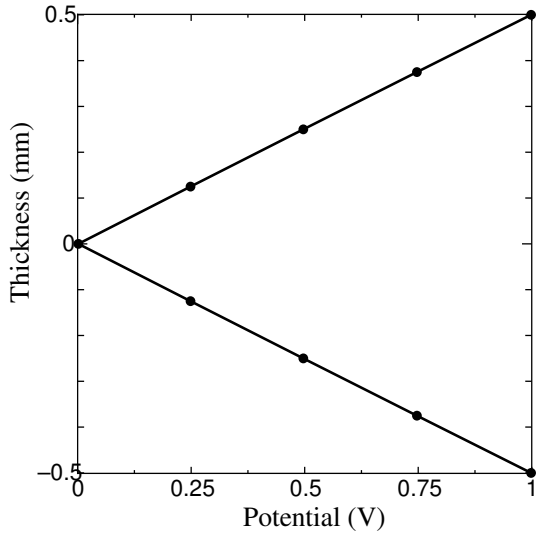
(b) A parallel connection piezoelectric bimorph actuator.

Fig. 15. Variation of the electric potential across the thickness in a piezoelectric bimorph actuator.

Fig. 16. Static deflection of the bimorph actuator.

the electrical and mechanical fields using the solid elements [27] and the static deflection obtained in the shell elements from the electric forces and moments applied externally to the shell elements. These results demonstrate very good agreement among the static deflection from the piezoelectric effect obtained using the solid–solid element analysis, the shell elements for the structural analysis, and the theory Eq.(33) [18]. This indicates that the induced electric force and the moment of the electric forces are accurately transformed from the solid elements to the shell elements using the proposed method.

The motional restrictions along the joined surfaces of the two piezoelectric layers creates forces and moments that result in the pure bending of the piezoelectric bimorph actuator. The total moment of the electric forces in the solid elements due to the piezoelectric effect obtained using the BGS algorithm [27] is $M_{eq} = 1.1506 \times 10^{-8}$ Nm. The relative error of the numer-

ical solution with respect to the theoretical solution is 0.052%. The deflection of the bimorph solved using piezoelectric solid elements [27] and that solved using shell elements show good agreement, demonstrating the accurate transformation of the forces and moments.

3.4. Dynamic analysis of bimorph actuator

3.4.1. AC response

The bimorph actuator shown in Fig. 9 was examined under AC input voltages with $\phi = \phi_0 \sin\omega_\phi t$, where ω_ϕ and ϕ_0 are the frequency and amplitude of the input voltage, respectively. The values of β and γ for the Newmark integration were selected as $\beta = 0.25$ and $\gamma = 0.5$. The time increment was set to $\Delta t = (1/50)(2\pi/\omega_\phi)$ for input frequencies much smaller or larger than the resonance frequency and $\Delta t = (1/200)(2\pi/\omega_\phi)$ for input frequencies near resonance to obtain the converged vibration amplitudes [27]. A finer time resolution was used near resonance because the deflection is very sensitive to changes in the frequency near resonance.

Fig. 17 show the iteration convergence properties of the BGS and full N–R iterations in the dynamic analysis using Approach 1 for a bias voltage of $\phi = 1$ V at a frequency of $\omega_\phi = 106$ rad/s and a time increment of $\Delta t = 3.0 \times 10^{-4}$ s. Figures 17(a)–c) shows the increment in internal energy during each N–R iteration at every BGS iteration. According to Fig. 17(a), in the first BGS iteration at every time step, three or four N–R iterations were executed before the preassigned energy tolerance criterion was satisfied. Similarly, in the second and third BGS iterations, only one N–R iteration was required to reach convergence, as shown in Fig. 17(b) and (c), respectively. The relative error of the tip deflection at every BGS iteration is shown in Figures 17(d)–f). The BGS iteration convergence is obtained based on the relative error between the previous and the current iteration solution in the dynamics analysis. As shown in Fig. 17(d) and (e), the tip deflection did not

13

(a) First BGS iteration.   **(b)** Second BGS iteration.   **(c)** Third BGS iteration.

(d) First BGS iteration.   **(e)** Second BGS iteration.   **(f)** Third BGS iteration.
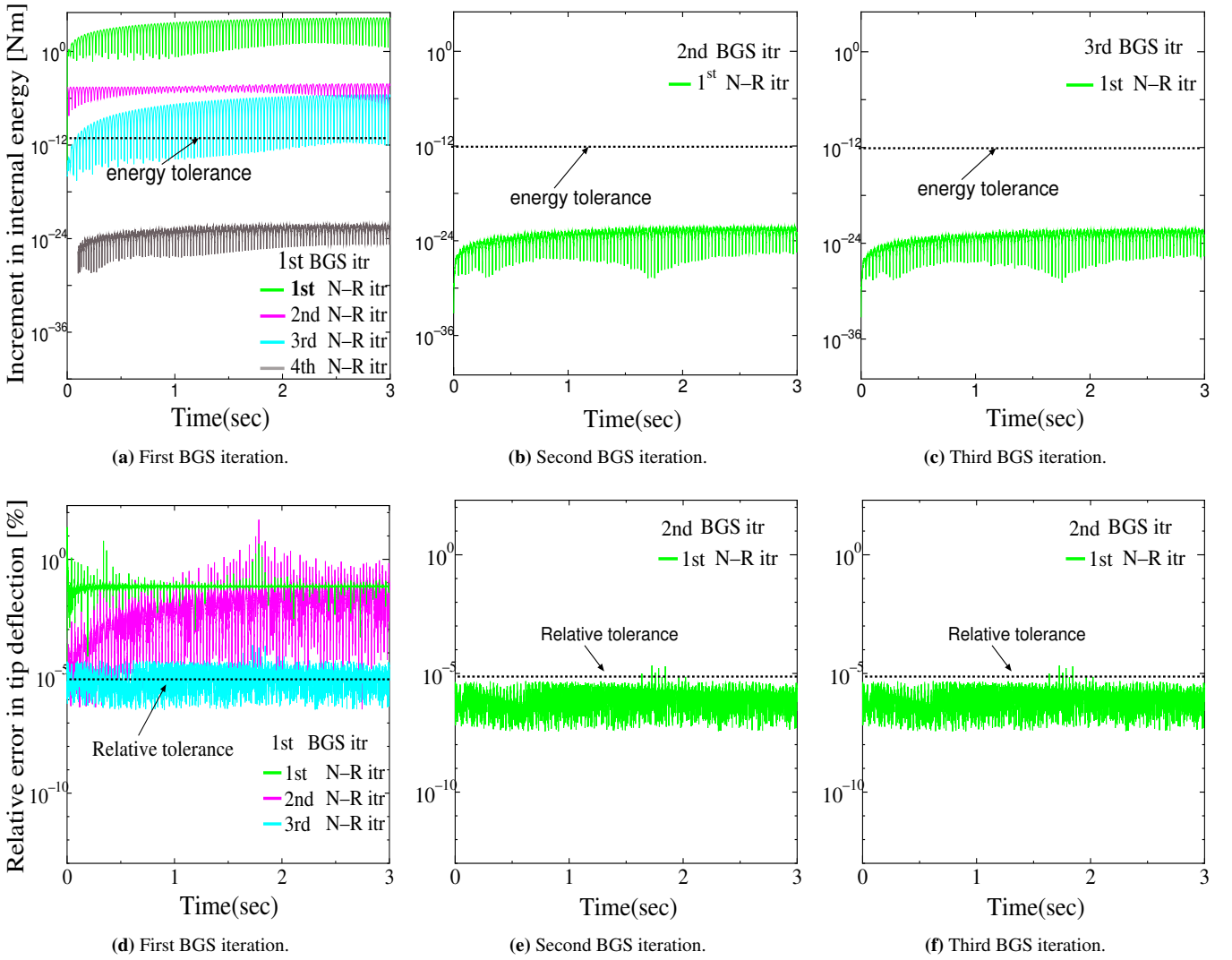
Fig. 17. Dynamic analysis iteration convergence properties: Approach 1. The energy tolerance and tip deflection relative error is plotted against the time at every BGS iterations.

converge to the preassigned relative tolerance value in first and second BGS iterations; in contrast, the relative error of the tip deflection satisfied the tolerance criteria at every time step in the third BGS iteration, as shown in Fig. 17(f).

Next, the vibration characteristics of the tip of the piezoelectric bimorph actuator in response to input AC signals with different frequencies and an amplitude of $\phi = 1$ V obtained using Approach 1 are depicted in Fig. 18. The peak displacements of the AC responses to the input signals with the different frequencies are summarized in Fig. 19. The point of maximum deflection at the tip of the bimorph actuator indicates when the frequency of the input voltage is equal to the resonance frequency of the actuator.

The responses of the actuator at input voltage frequencies of $\omega_\phi = 107.0$, 107.1, and 107.2 rad/s, which are close to the structural resonance frequency, had large amplitudes [29], as shown in Fig. 19; however, for input voltage frequencies much larger or smaller than the structural resonance frequency, the peak am-

plitudes of the responses were approximately equivalent to the tip deflection under a static force [29], as shown in Fig. 18(a) and (d). The response in Fig. 18(c) achieved the largest peak amplitude among the different input frequencies, indicating resonance was achieved at this frequency. Fig. 19 reveals that the simulation results yielded a maximum peak deflection amplitude at an input voltage frequency of $\omega_\phi = 106.90$ rad/s. The resonance of the piezoelectric bimorph actuator actually occurs at a driving input voltage frequency very close to the theoretical frequency of $\omega_r^{(1)} = 107.0$ rad/s. Therefore, the numerical and theoretical solutions are in good agreement with each other.

The AC response was then simulated using Approach 2. Fig. 20(a) shows the vibration characteristics at an input voltage frequency much smaller than the structural resonance frequency of the bimorph actuator. There is an instability in the solution when one BGS iteration is performed in each time step; however, there is no such instability when two or more BGS iterations are used in each time step. The instability appears for the
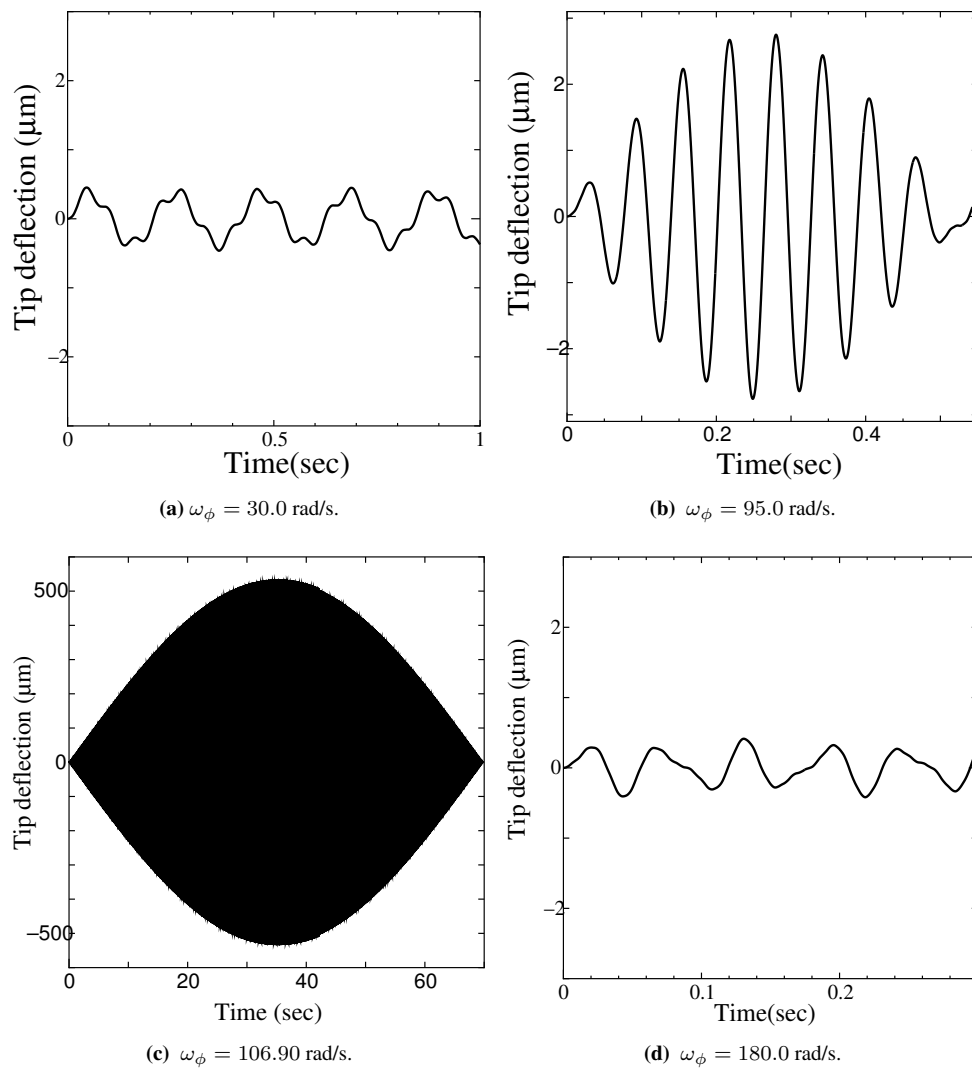
(a) $\omega_\phi = 30.0$ rad/s.

(b) $\omega_\phi = 95.0$ rad/s.

(c) $\omega_\phi = 106.90$ rad/s.

(d) $\omega_\phi = 180.0$ rad/s.

Fig. 18. AC response of a bimorph actuator in a series connection at different frequencies simulated using Approach 1.

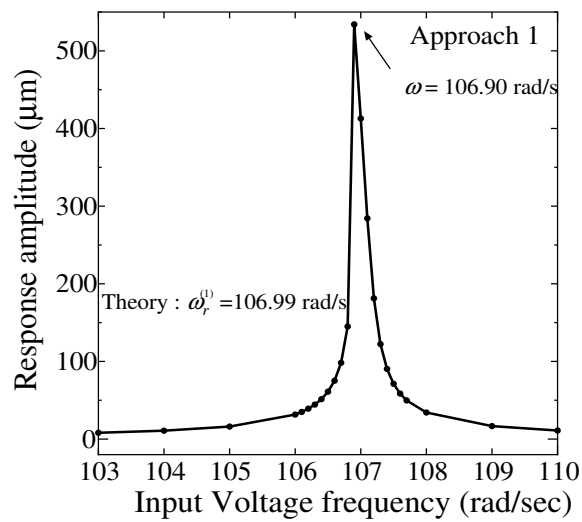**Fig. 19.** Frequency response curve of a bimorph actuator calculated using Approach 1.
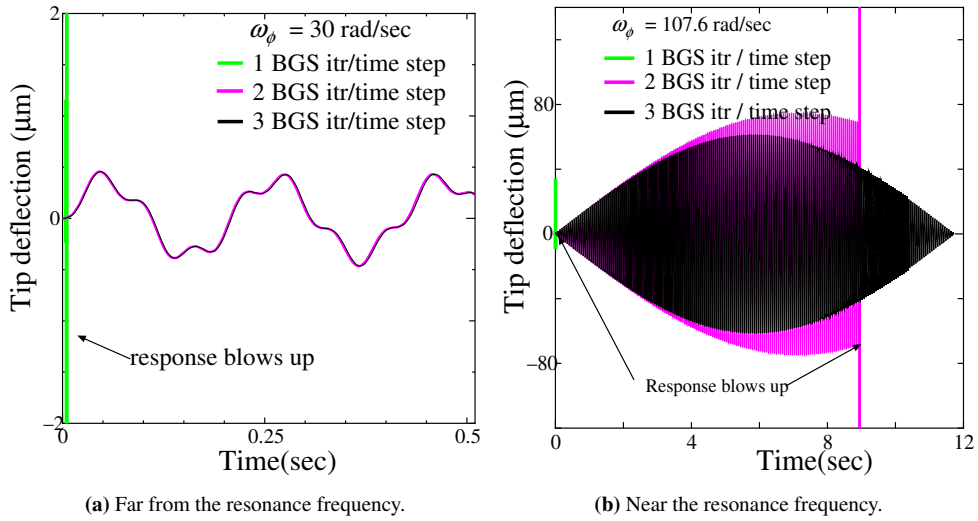
(a) Far from the resonance frequency.

(b) Near the resonance frequency.

Fig. 20. AC response of a bimorph actuator in a series connection at different frequencies simulated using Approach 2.

(a) Tip deflection iteration convergence.

(b) The internal energy increment obtained after N–R and BGS iteration for each time step.
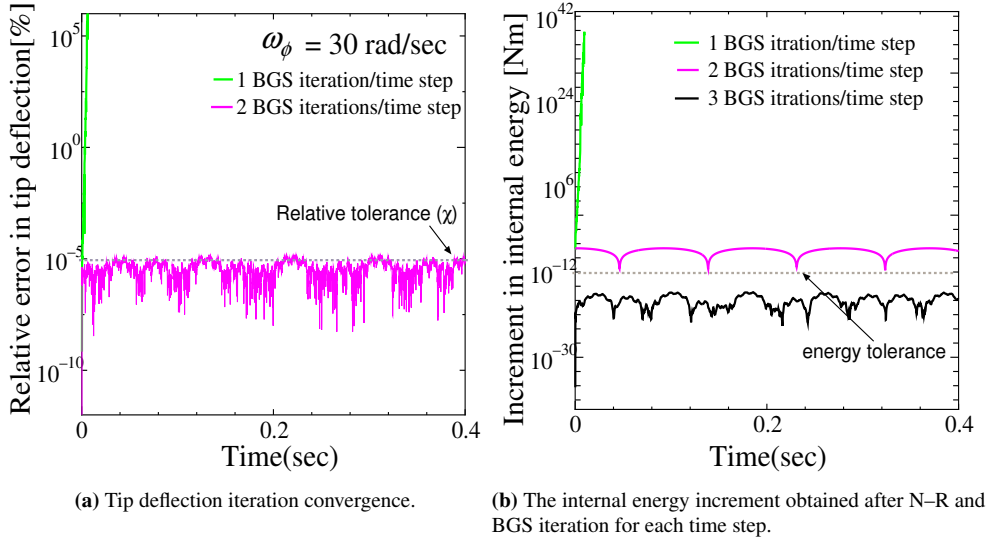
Fig. 21. Dynamic analysis iteration convergence properties: Approach 2.

unified algorithm for input frequencies far away from the resonance if only one nonlinear iteration is used. The source of this instability is the unconverged nonlinear solution. The residual of the nonlinear equation will be increased in the time steps, and nonlinear iterations more than two reduces such residual in the numerical solution. Also note that, when the input voltage frequency is close to the structural resonance frequency, an instability arises when one or two BGS iterations are used in each time step, as shown in Fig. 20(b). The reason for the instability that arises when the input voltage frequency is much smaller than the resonance frequency and one BGS iteration is used is delineated in Fig. 21. The relative error of the tip deflection approaches infinity when one BGS iteration is used in this case, as shown in Fig. 21(a). This is because the energy tolerance in the nonlinear N–R iteration is not satisfied when only one BGS iteration is applied, as shown in Fig. 21(b). From this assessment,

it is apparent that executing three or four nonlinear iterations in every time step would yield a converged solution without any instability when Approach 2 is used. If both the energy tolerance and relative tolerance are introduced then we obtain stable solution, as shown in the results. Since this approach requires less number of nonlinear iterations than the first approach, it is computationally efficient than the first approach. The vibration amplitudes at various AC input voltages are approximately equal to those obtained using Approach 1. The same level of accuracy was achieved in both approaches.

3.4.2. Step response of a piezoelectric bimorph actuator

The vibration characteristics of the piezoelectric bimorph actuators driven by a step voltage $\phi = 1$ V obtained using Approach 1 are presented here. Newmark [68] presented a numerical damping scheme in which $\beta = 0.25(\gamma+0.5)^2$ with $\gamma > 0.5$;

16

on the basis of this method, a step input voltage with the New-mark parameters of $\gamma = 0.6$ and $\beta = 0.3025$ was used to obtain steady-state equilibrium after a long time interval. These parameters were adopted because when a bimorph actuator is actuated with numerically positive damping with a step input bias voltage, the steady-state response of the tip deflection is equal to the theoretical solution for the static deflection. The time increment Δt was chosen as 1.0×10^{-3} s.

Fig. 22 shows the step response of the numerical problem in Fig. 9. The steady-state tip deflection was obtained as $0.3452\,\mu$m, whereas the theoretical static tip deflection obtained from Eq.(33) is $u_3(L) = 0.3450\,\mu$m. Thus, the relative error of the tip deflection is 0.057%. The exact value of the natural period of vibration ($T_n = 1/f_r$) for this problem is 0.0587 s, where the natural frequency f_r is obtained using Eq.(35). The obtained natural period using the numerical analysis is 0.0585 s. The natural period of vibration showed good agreement between the numerical and theoretical solution. Highly accurate solutions were obtained using the proposed coupled algorithm. Approach 2 yielded similar results.

4. A piezoelectric bimorph sensor mode

4.1. Problem setup

Many piezoelectric shell formulation in Refs. [55, 56] are limited to only actuator function, so they can not solve sensor problems. In this section, the sensor response of a piezoelectric bimorph cantilever shown in Fig. 23 is obtained for a transverse load F at the free end of the shell structure, as shown in Fig. 23 (a). The nodes with the electric degree of freedom (DOF) at the top, bottom, and mid–surfaces of a piezoelectric bimorph FE model are regarded as an electrode. Four electrical configurations are analyzed:

1. Closed circuit configuration (active mode): The nodes at the top and bottom surfaces are set to zero electric potential, as shown in Fig. 23(b).

2. Closed and open circuit configuration (active–sensory mode): The nodes at the top surface are in an open circuit condition while the bottom surface is earthed, as shown in Fig. 23(c). Some piezoelectric shell formulations in Refs. [15, 42, 53, 58–60] can be used to model both the actuator and sensor function of piezoelectric bimorph, provided one or two equipotential electrodes (ex. active mode). Since the electric potential serves as unknowns in an active–sensory configuration, they are modeled with a linear variation of the electric potential through the thickness [53], which leads to quite a wrong solution because the electromechanical coupling would be partial and would neglect the induced potential in sensor mode, as discussed in [20]. On the other hand, the proposed method can take into account the quadratic variation of electric potential in active–sensory configuration.

3. Partial open circuit configuration: In this configuration, a node at the top and bottom surface near the fixed end are grounded while other nodes are in open circuit configuration, as shown in Fig. 23(d).
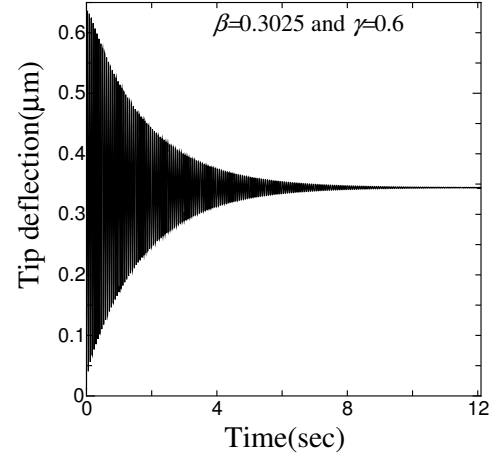

Fig. 22. Response of a bimorph actuator to a step input voltage.

4. Full open circuit configuration (sensory mode): Both the top and bottom surfaces are in an open circuit condition, as shown in Fig. 23(e). In energy harvesting application, open surfaces at the bottom and top are general [10, 11].

From the formulation viewpoint, the piezoelectric shell proposed in [53] cannot solve active sensory configuration (Fig. 23(c)), partial open circuit configuration (Fig. 23(d)), and full open circuit configuration (Fig. 23(e)), because, in the piezoelectric shell, the potential at the mid–plane nodes is unknown, both top and bottom surface electrode potential must be prescribed to determine quadratic variation. This makes the usage of the piezoelectric shell very difficult in the piezoelectric bimorph sensor analysis. Using our proposed method, the quadratic variation in active sensory configuration, partial open circuit configuration, and full open circuit configuration can be achieved.

The piezoelectric bimorph beam shown in Fig. 23 has a length of $L = 250$ mm, a width of $w = 20$ mm, and a thickness of each layer $t_p = 2.5$ mm. The piezoelectric layers are polarized in the same direction along the thickness. All the mechanical DOF are fixed at $x = 0$. The mesh for the structural analysis consists of MITC4 shell elements with the numbers of nodes and elements totaling 22 and 10, respectively. The mesh for the electric analysis consists of 20-node hexahedral elements with the numbers of the nodes and elements totaling 353 and 40, respectively.

4.2. Static analysis of sensor function

The displacement of the tip due to a transverse load F at the free end of the shell structure produces a voltage in the 3D solid of the bimorph cantilever beam. For the rectangular bimorph cantilever sensor connected in parallel [69, 70] we have

$$V = \frac{3}{16} g_{31} E_p \frac{t^2}{L^2} \delta, \tag{37}$$

where V is the generated electric voltage, g_{31} is the piezoelectric voltage coefficients, and δ is maximum tip deflection due to pure mechanical transverse loading F at the tip. Piezoelectric voltage constant g_{31} for a PVDF material is 0.216 Vm/N.
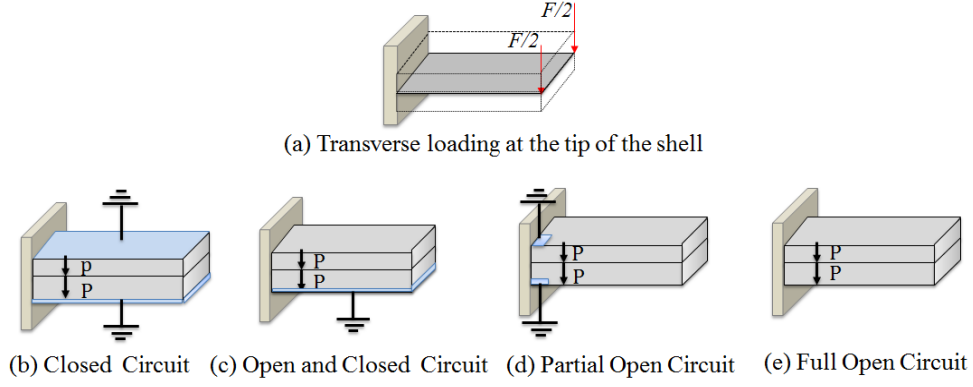
(a) Transverse loading at the tip of the shell

(b) Closed Circuit   (c) Open and Closed Circuit   (d) Partial Open Circuit   (e) Full Open Circuit

Fig. 23. Piezoelectric bimorph cantilever sensor configuration:

(a) Closed circuit configuration

(b) Active–sensory mode configuration

(c) Partial open circuit configuration

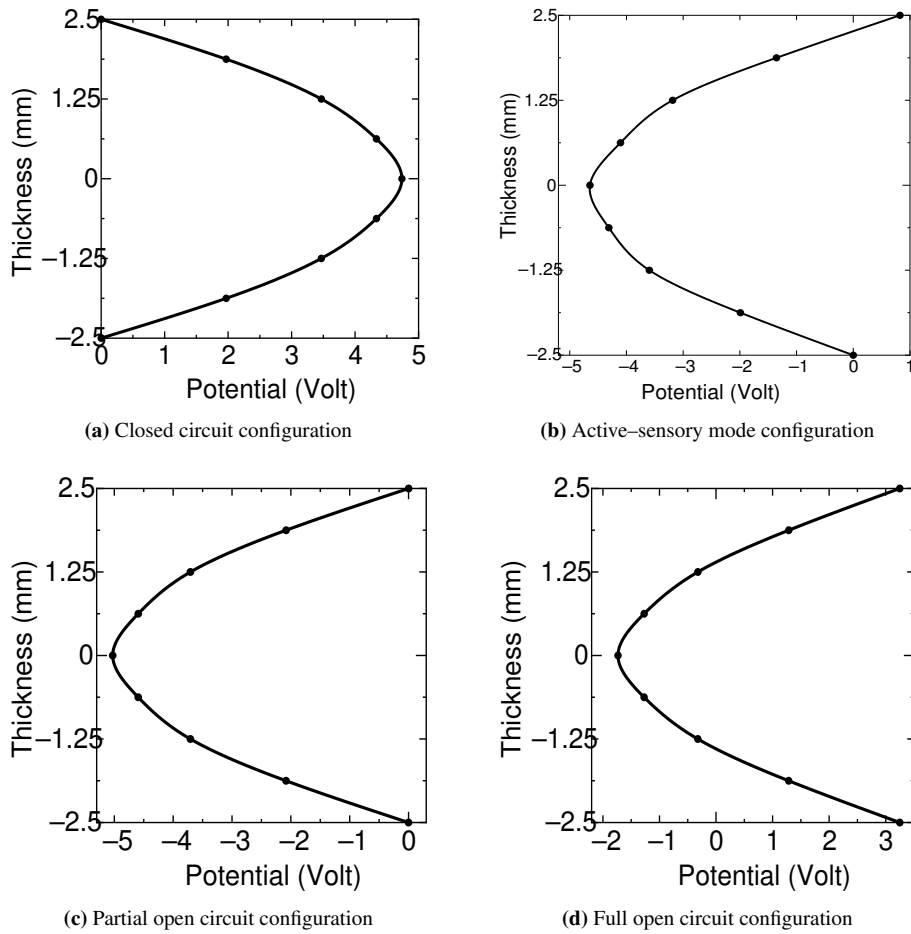

(d) Full open circuit configuration

Fig. 24. Distribution of potential over the thickness of the bimorph cantilever for sensor model under $F = 1 \times 10^{-3}$ N.

The maximum tip deflection δ for an applied tip load F is obtained using,

$$\delta = \frac{FL^3}{3E_pI}. \tag{38}$$

Taking tip load $F = 1 \times 10^{-3}$ N, the numerical results of the distribution of induced electrical potential over the thickness at $x = 0, y = 0$ are presented in Fig. 24. It is apparent from Fig. 24 that the induced electrical potential obtained

with the FE analysis varies, almost quadratically over the thickness. It is easily understood that the potential in the upper and lower surfaces is zero for closed circuit electric configuration, as shown in Fig. 24(a). Similarly, there exists a potential on the top surface while it is zero on the bottom surface for active–sensory mode configuration, as shown in Fig. 24(b). The theoretical solution has a value $V = 0.8647$V for applied tip load $F = 1 \times 10^{-3}$ N while the numerical solution using proposed method is $V = 0.8471$V, shown in Fig. 24(b). The numerical

18

solutions agree well with the theory. The induced electric potential for the partial open circuit and full open circuit sensor configuration is shown in Figures 24(c) and 24(d). As shown in Fig. 24(d), it is clear that for the full open circuit configuration, the induced electric potential on both the top and bottom surface is same and has a value $V = 3.2484$ volts for applied tip load $F = 1 \times 10^{-3}$ N. As presented here, the 3D solid elements in sensor mode can model the electric field under any electric boundary conditions with almost a quadratic variation of the induced electric potential over the thickness.

Fig. 25 shows the maximum induced electric potential in the solid elements for an active–sensory circuit configuration versus applied tip load at the shell elements compared with the theoretical solution, and solid–solid [27]. The solution obtained with the proposed method is in good agreement with the theory and linear solid–solid in the elastic region. The proposed shell–solid method shows nonlinear behavior which can not be analyzed using theory.

5. Conclusions

A new finite element scheme for the simulation of the piezoelectric interaction between the structure and electrical fields was developed using a combination of both solid and shell elements for the finite element model. The field decomposition employed in this method enables the use of different elements to solve the different fields. A novel method of exchanging the electric force, the moment of the electric force, and the displacement between the electrical field in the solid elements and the mechanical field in the shell elements was developed. The proposed method can be used to analyze both the actuator and sensor function in a thin-layered piezoelectric bimorph cantilever of various electric configurations with both the linear and quadratic variations of the electric potential across the thickness direction.

The geometric nonlinear structure-electric interaction of the piezoelectric effect was analyzed by applying two approaches. In the first approach (i.e. BGS iteration with the N–R loop), the N-R iteration loop is executed in every BGS iteration until the convergence criteria are satisfied. In the second approach (i.e. unified approach), the BGS iteration and N–R iteration loops are unified to single loop. From the viewpoint of computational cost, the second approach is computationally efficient. Both the approaches show the same level of accuracy.

The proposed coupling scheme is well suited for use in the general–purpose FEA of the thin piezoelectric bimorph in MEMS. It was shown that using a combination of solid and shell elements to solve the electrical and structural fields, respectively, with the proposed method of transforming the force, moment, and displacement between the two fields allows for the very accurate simulation of the general electromechanical coupling or both the actuation and the sensing that occurs in the piezoelectric effect. The proposed method accurately takes into account the geometric nonlinear effect in both the actuator and sensor mode.
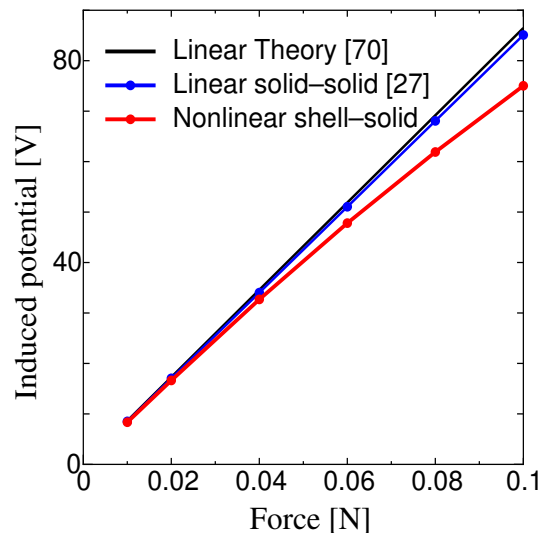

Fig. 25. Maximum induced electric potential v/s applied tip load for active–sensory configuration of piezoelectric bimorph cantilever connected in parallel.

References

[1] J.Curie, P. Curie, Development via compression of electric polarization in hemihedral crystals with inclined faces, Bull Soc Minral 1880 :90–93.

[2] K. Uchino, Piezoelectric actuators/ ultrasonic motors – their developments and markets, Proc of 1994 IEEE Int Symp Appl Ferroelectr 1995; 319–324.

[3] C.B. Eom, S. Trolier-McKinstry, Thin-film piezoelectric mems, Mater Res Soc Bull 2012; 37 (11) :1007–1017.

[4] Q.M. Wang, L.E. Cross, Performance analysis of piezoelectric cantilever bending actuator, Ferroelectrics 1998; 215 (1) :187–213.

[5] H.S. Tzou, Development of a light-weight robot end-effector using polymeric piezoelectric bimorph, Proc IEEE Int Conf Robot Autom 1989; 3 :1704–1709.

[6] C.I. Tseng, Electromechanical dynamics of a coupled piezoelectric/mechanical systems applied to vibration control and distributed sensing, Ph.D Dissertation, Univ. of Kentucky, Lexington, Ky. July, 1989;.

[7] Z. Wang, S. Chen, W. Han, The static shape control for intelligent structures, Finite Elem Anal Des 1997; 26 (4) :303–314.

[8] C. Lee, T. Itoh, T. Suga, Micromachined piezoelectric force sensors based on pzt thin films, IEEE Trans Ultrasonics, Ferroelect Freq Control, 1996; 43 :553–559.

[9] T. Shibata, K. Unno, E. Makino, S. Shimada, Fabrication and characterization of diamond afm probe integrated with pzt thin film sensor and actuator, Sens Actuators A: Phys 2004; 114 (2–3) :398–405.

[10] A. Erturk, D.J. Inman, An experimental validated bimorph cantilever model for piezoelectric energy harvesting from base excitation, Smart Mater.Struct 2009; 18 :025009, 15 pages.

[11] Y. Tanaka, T. Oko. H. Mutsuda, A.A. Popov, R. Patel, S.M. William, Forced vibration experiments on flexible piezoelectric devices operating in air and water environments, Int J Appl Electrom 2014; 45 :573–580.

[12] R.J. Wood, B. Finio, M. Karpelson, K. Ma, N.O. Perez-Arancibia, P.S. Sreetharan, H. Tanaka H, J.P Whitney, Progress on pico air vehicles, Int J Robot Res 2012; 31 (11) :1292–1302.

[13] D. Ishihara, N. Ohira, M. Takagi, T. Horie, Fluid-structure interaction design of insect-like micro flapping wing, Proc of the VII Int Conf Computational Methods for Coupled Problems In Science and Engineering (Coupled Problems 2017), Greece :870–875.

[14] D. Ishihara, T. Horie, M. Denda, A two dimensional computational study on fluid-structure interaction cause of wing pitch changes in dipteran flapping flight, J Exp Biol 2009; 212 :1–10.

[15] M. Kogli, M.L. Bucalem, Analysis of smart laminates using piezoelectric mitc plate and shell elements, Comput Struct 2005; 83 (15–16) :1153–1163.

[16] S.Y. Wang, A finite element model for the static and dynamic analysis of a piezoelectric, Int J Solids Struct 2003; 41 (15) :4075–4095.

[17] A. Fernandes, J. Pouget, Analytical and numerical approaches to piezoelectric bimorph, Int J Solids Struct 2003; 40 :4331–4352.

[18] J.G. Smits, A. Ballato, Dynamic admittance matrix of piezoelectric cantilever bimorphs, J Microelectromech Syst 1994; 3 (3) :105 – 112.

[19] S. Kapuria, P. Hangedorn, Unified efficient layerwise theory for smart beams with segmented extensio/shear mode, piezoelectric actuators and sensors, J Mech Mater Struct 2007; 2 (7) :1267–1298.

[20] A. Benjeddou, Advances in piezoelectric finite element modeling of adaptive structural elements:a survey, Comput Struct 2000; 76 (1–3) :347–363.

[21] A. Benjeddou, J. Deu, S. Letombe, Free vibrations of simply–supported piezoelectric adaptive plates:an exact sandwich formulation, Thin–Walled Struct 2002; 40 :573–593.

[22] W. Zouari, B. Zineb, A. Benjeddou, A fsdt-mitc piezoelectric shell finite element with ferroelectric non-linearity, J Intell Material Syst Struct 2009; 20 (17) :2055–2075.

[23] M. Kogli, M.L. Bucalem, A family of piezoelectric mitc plate elements, Comput Struct 2005; 83 :1277–1297.

[24] O.Z. Zienkiewicz, R.L. Taylor, The finite element method, fifth edition, volume 1 : The basis, Butterworth-Heinemann 2000.

[25] D. Ishihara, T. Horie, T. Niho, T. Baba, Hierarchal decomposition for the structure-fluid-electrostatic interaction in a microelectromechanical system, Comput Model Eng Sci 2015; 108 (6) :429–452.

[26] P.C. Ramegowda, D. Ishihara, T. Niho, T. Horie, A finite element approach for a coupled numerical simulation of fluid -structure-electric interaction in mems, Proc of the VII Int Conf Computational Methods for Coupled Problems In Science and Engineering (Coupled Problems 2017), Greece :999–1007.

[27] P.C. Ramegowda, D. Ishihara, T. Niho, T. Horie, Performance evaluation of numerical finite element coupled algorithms for structure-electric interaction analysis of mems piezoelectric actuator, International Journal of Computational Methods 2018; 15 (3) :1850106, 28 pages.

[28] P.C. Ramegowda, D. Ishihara, R. Takata, T. Niho, T. Horie, Fluid–structure and electric interaction analysis of piezoelectric flap in a channel using a strongly coupled fem scheme, Proc of the 6th European Conference on Computational Mechanics (Solids, Structures and Coupled Problems), Glasgow, 2018 :382–393.

[29] F. Shi, P. Ramesh, S. Mukherjee, Dynamic analysis of micro electro mechanical systems, Int J Numer Meth Engng 1996; 39 (24) :4119–4139.

[30] V. Rochus, D.J. Rixen, J.C. Golivnal, Non-conforming element for accurate modelling of mems, Finite Elem Anal Des 2007; 43 :749–756.

[31] V. Rochus, C. Geuzaine, A primal/dual approach for the accurate evaluation of the electromechanical coupling in mems, Finite Elem Anal Des 2012; 49 :19–27.

[32] H. Allik, T.J.R. Hughes, Finite element method for piezoelectric vibration, Int J Numer Meth Engngng 1970; 2 :151–157.

[33] H. Allik, M.W. Kenneth, T.H. John, Vibrational response of sonar transducer using piezoelectric finite elements, J Acoust Soc Am 1974; 56 :1782–91.

[34] H.S. Tzou, C.I. Tseng, Distributed piezoelectric sensor/actuator design for dynamic measurement/control of distributed parameter systems:a piezoelectric finite element approach, J Sound Vibr 1990; 138 (1) :17–34.

[35] H.S. Tzou, C.I. Tseng, H. Bahrami, A piezoelectric hexahedron finite element applied to design a smart continua, Finite Elem Anal Des, 16: (1994) 27–42.

[36] L.C. Chin, V.V. Varadan, V.K. Naradan, Hybrid finite element formulation for periodic piezoelectric arrays subjected to fluid loading, Int J Numer Meth Engng 1994; 37 (1) :2987–3003.

[37] K. Ghandi, N.W. Hagood, Nonlinear finite element modeing of phase

transitions in electro-mechanically coupled material, Smart Struct Mater: SPIE 1996; 2715 :121–140.

[38] K. Ghandi, N.W. Hagood, A hybrid finite element modelfor phase transition in nonlinear electro-mechanically coupled material, Smart Struct Mater: SPIE 1997; 3039 :97–112.

[39] S.K. Ha, C. Keilers, F.K. Chang, Finite element analysis of composite structures containing distributed piezoelectric sensors and actuators, AIAA J 1992; 30 :772–780.

[40] R. MacNeal, R. Harder, A proposed standard set of problems to test finite element accuracy, Finite Elem Anal Des 1985; 1 :3–20.

[41] I.S. KoKo, I.R. Orisamolu, M.J. Smith, U.O. Alepan, Finite element based design tool for smart composite structures, Smart Struct Mater:SPIE 1997; 3039 :125–134.

[42] R. Lammering, The appllicaton of a finite shell element for composites containing piezoelectric polymer in vibration control, Comput Struct 1991; 41 (5) :1101 – 1109.

[43] T.A. Quentin, D.J. Brian, L.L. Howell, Geometrically non-linear analysis of thin-film compliant mems via shell and solid elements, Finite Elem Anal Des 2012; 49 :70–77.

[44] W.S. Hwang, H.C. Park, Finite element modeling of piezoelectric sensors and actuators, AIAA J 2013; 31 (5) :930–9937.

[45] H. Noguchi, T. Hisada, Sensitivity analysis in post buckling problems of shell structures, Comput Struct 1993; 47 (4-5) :699–710.

[46] E.N. Dvorkin, K.J. Bathe, A continuum mechanics based four-node shell element for general nonlinear analysis, Eng Comput 1984; 1 (1) :77–88.

[47] K.J. Bathe, E.N. Dvorkin, A formulation of general shell elements-the use of mixed interpolation of tensorial components, Int J Numer Meth Engngng 1986; 22 (3) :697–722.

[48] V.V. Varadan, L.C. Chin, V.K. Naradan, Finite element modeling of flextensional electroacoustic transducers, Smart Mater Struct 1993; 2 (4) :201–207.

[49] N. Guo, P. Cawley, D. Hitchings, The finite element analysis of the vibration characteristics of piezoelectric discs, J Sound Vibr 1992; 159 (1) :115–138.

[50] R. Lammering, R.S. Mesecke, Multi-field variational formulations and related finite elements for piezoelectric shells, Smart Mater Struct 2003; 12 (12) :904–913.

[51] V.D. Varelis, D.A. Saravanos, Coupled mechanics and finite element for non-linear laminated piezoelectric shallow shells undergoing large displacements and rotations, Int J Numer Meth Engng 2006; 66 (8) :1211–1233.

[52] R. Zemk, R. Rolfes, M. Rose, J. Tessmer, High-performance four-node shell element with piezoelectric coupling for the analysis of smart laminated structures, Int J Numer Meth Engng 2007; 70 (8) :934–961.

[53] D. Lenger, S. Klinkel, W. Wagner, An advanced finite element formulation for piezoelectric shell structures, Int J Numer Meth Engng 2013; 95 (11) :901– 927.

[54] X. Wang, Y. Wang, On non-linear behaviour of spherical shallow shells bonded with piezoelectric actuators by the differential quadrature element method (dqem), Int J Numer Meth Engng 2002; 53 (6) :1477–1490.

[55] R. Iozzi, P. Gaudenzi, Effective shear deformable shell elements for adaptive laminate structures, J Intell Mater Syst Struct 2001; 12 (6) :415–422.

[56] A. Zallo, P. Gaudenzi, Finite element models for laminated shells with actuation capability, Comput Struct 2003; 81 :1059– 1069.

[57] X. G. Tan, L. Vu-Quoc, Optimal solid shell element for large deformable composite structures with piezoelectric layers and active vibration control, Int J Numer Meth Engng 2005; 64 :1981–2013.

[58] V. Balamurugan, S. Narayanan, Shell finite element for smart piezoelectric composite plate/shell structures and its application to the study of active vibration control, Finite Elem Anal Des 2001; 37 :713–738.

[59] D.A. Saravanos, Mixed laminate theory and finite element for smart piezoelectric composite shell structures, AIAA J 1997; 35 (8) :1327–1333.

[60] M. Kogli, M.L. Bucalem, Locking free piezoelectric shell elements. in bathe kj editor, Computational Fluid and Solid Mechanics. Elsevier 2003; (15–16) :392–395.

[61] C.A. Felippa, K.C. Park, C. Farhat, Partitioned analysis of coupled mechanical system, Comput Meth Appl Mech and Engng 2001; 190 :3247–3270.

[62] J. Fish, W. Chen, Modeling and simulation of piezocomposites, Comput Meth Appl Mech and Engng 2003; 192 (28–30) :3211 – 3232.

[63] P. Gaudenzi, K.J. Bathe, An iterative finite element procedure for the analysis of piezoelectric continua, J Intell Mater Syst and Struct 1995; 6 (2) :226–273.

[64] K.J. Bathe, Finite element procedures 2006, Prentice-Hall,.

[65] K.J.Bathe, E.Ramm, E.L.Wilson, Finite element formulation for large deformation dynamics analysis, Int J Numer Meth Engngng 1975 9 (2) 353–386.

[66] M.L. Bucalem, K.J. Bathe, Finite element analysis of shell structures, Arch Comput Meth Eng, 4: (1997) ,3–61.

[67] K.J. Bathe, A.P. Cimento, Some practical procedures for the solution of nonlinear finite element equations, Comput Meth Appl Mech and Engng 1980; 22 (1) :59–85.

[68] N.M. Newmark, A method of computation for structural dynamics, Proc Am Soc Civil Eng J Eng Mech Div 1959; 85 (3) :67–94.

[69] C.P. Germano, Flexural mode piezoelectric transducers, IEEE Trans Audio Elecroacoustics 1971; 19 :6–12.

[70] P. Kielzynski, W. Pajewski, M. Szalewski, Piezoelectric sensors for investigations of microstructures, Sens Actuators A: Phys 1998; 65 :13–18.